

**Systematic characterization of a Geiger-mode
micro-pixel avalanche photo-diode for
cryogenic operation and application to liquid
Argon TPCs**

Master Thesis

der Philosophisch-naturwissenschaftlichen Fakultät

der Universität Bern

vorgelegt von

Sébastien Claude Delaquis

2010

Leiter der Arbeit:

Prof. Dr. Antonio Ereditato

Dr. Igor Kreslo

Albert Einstein Center for Fundamental Physics
Laboratorium für Hochenergiephysik

Abstract

A micro-pixel avalanche photo-diode operated in Geiger-mode (G-MAPD) has been systematically characterized at three different temperatures (298 K, 87 K, 77 K). The gain, noise-rate and cross-talk were measured. It was found that the G-MAPD is well suited as a single-photon counting device for cryogenic conditions.

In high energy physics Time Projection Chambers (TPCs) are nowadays used as particle tracking detectors. For the search of Dark Matter and neutrino interactions, low threshold TPC readout is an important issue. Having a G-MAPD working at low temperatures opens new possibilities in this field.

In the framework of this thesis, a novel prototype TPC readout-system, the hybrid-field-induced-emission-amplifier (HFIE), was partially explored for use in Argon gas. To do so a HFIE, including a dewar, a small drift-chamber, a DAQ system and the related software, was realized and operated at the Laboratory for High Energy Physics (LHEP) in Bern.

Contents

Introduction	1
1 Photon detectors	3
1.1 The photomultiplier tube	4
1.2 Semiconductor photon detectors	6
2 Experimental set-up, data taking and processing	15
2.1 Set-up	15
2.2 Measuring procedures	17
2.3 Data processing	20
2.4 Specifications of the "MAPD-3N" at cryogenic conditions	27
3 Cryogenic TPC readout system with a G-MAPD	29
3.1 The TPC and its readout systems	30
3.2 The HFIE prototype, a novel approach of TPC readout	35
4 Conclusions and outlook	45
A Construction of the automatic level regulating valve	47
B Construction of the μ-Ar-Tube	51
List of figures	60
Bibliography	63

Introduction

A Geiger-mode micro-pixel avalanche photo-diode (G-MAPD) is a semiconductor solid-state photon detector. Distinct to conventional avalanche-photo-diodes (APD), the G-MAPD works with a reversed bias-voltage above the breakdown-voltage, in the so-called Geiger-mode. In this mode all the cells (pixels) of the G-MAPD are in a metastable state where a single electron-hole pair starts a self sustaining avalanche in its cell. The avalanche needs to be quenched by lowering the bias voltage below the breakdown voltage (e.g. by a surface resistor for each cell). This leads to a quasi-digital response of the G-MAPD to the number of cells triggered. The gain achieved by this mechanism is much larger (in the range of 10^5 to 10^7) than for conventional APDs (between 50 and 200). Thus G-MAPDs can detect single photons as well as photo multiplier tubes (PMT), and are therefore sometimes also called silicon-photo-multipliers (SiPM).

The Time Projection Chamber (TPC) is a particle detector that allows three-dimensional tracking of ionizing particles. Since the 70's TPCs filled with gas or liquids are used in particle physics experiments providing high spatial resolution of the particle tracks. In most cases, gaseous or liquefied noble gases such as Argon and Xenon are used due to their excellent chemical features. Considering cost and availability, the liquid Argon TPC technique is very promising. AS an example, it is one of three leading options for a future large underground detector in the LAGUNA project (Large Apparatus for Grand Unification and Neutrino Astrophysics).

To visualize the charge track left behind by the ionizing particle different TPC readout-systems are commonly used. The hybrid-field-induced-emission amplifier (HFIE) is a novel approach of TPC readout-system. In the drift-field of a TPC the electrons of the ionizing track are drifted towards the readout-device. Reaching the HFIE these electrons are accelerated in a high electric field (amplification-field) generating secondary scintillation in gas or liquid. The scintillation light is then collected with a G-MAPD. One of the main advantages of this technique is its early state amplification. Low threshold TPC readout can be achieved by it, which is an important issue in the search of Dark Matter and in the measurement of neutrino interactions.

As a first step towards the HFIE a G-MAPD (the "MAPD-3N" from Zecotek) was systematically characterized at ambient and cryogenic temperatures. For this purpose an experimental set-up was realized including a valve to automatically control the level of the cryogenic liquids used. As a following step a HFIE including a dewar, a

small drift-chamber, a DAQ system and the related analysing software was realized at LHEP in Bern in the framework of this thesis's work. First measurements to prove the working principle of the HFIE were done in Argon gas.

Chapter 1

Photon detectors

In different applications many high energy physics experiments make use of photon detection. Since decades the photomultiplier tube (PMT) is a very popular choice to detect photons of low flux. A huge quantity of them were used in water-Cherenkov detectors in the experiments Kamiokande (around 1'000 PMTs) and Super Kamiokande (over 10'000 PMTs). PMTs also came to use in the sophisticated KamLAND detector (around 2'000 PMTs). Another prominent application of PMTs is by scintillation counter systems used in a wide range of experiments (e.g. for calorimeters, hodoscopes, triggers, etc.). An alternative device to the PMT are the semiconductor photo-diodes. But only after the recent development of the Geiger-mode micro-pixel avalanche photo-diode (G-MAPD) they have reached a sensitivity comparable with PMT's (see Table 1.1).

The evolution of the semiconductor photodiode started however in the sixties with the p-i-n photodiode (PIN). It is one of the simplest silicon photodiodes and is used in many applications (scintillation gamma calorimeters, active dosimeters, etc.) of today's elementary particle detectors. To detect single photons the PIN diode is however not suited due to the lack of internal gain.

To provide internal gain and thus higher sensitivity a new diode type was developed, the avalanche photo-diode (APD). Photo-electrons created in an APD are accelerated in an electric field, induced by an externally applied bias voltage. APD's work in the so-called linear-mode where the bias voltage is below the breakdown voltage. In this field the photo-electrons gain enough kinetic energy to create other electron-hole pairs leading to an electron avalanche. With this technique a moderate gain in the range of 50 to 200 is commonly achieved.

With a bias voltage very close to the breakdown voltage a much higher gain is theoretically possible. Operating an APD in this region is however very difficult due to the thermal dependence of the breakdown voltage and thermal electrons reaching the conductive band. APD's are not operated in this region except for the specially developed visual-light-photon-counter (VLPC). The VLPC is a very sensitive APD with single photon resolution. Yet it loses out by working only at very low (6 to 8 Kelvin) and accurate temperatures.

The real breakthrough in the striving for semiconductor photo-diodes with single photon resolution came with the invention of the G-MAPD. The G-MAPD works with a reversed bias voltage above the breakdown voltage, in the so-called Geiger-mode. Under these conditions APD's would immediately break down due to thermal electrons as mentioned before. The very small cells of the G-MAPD however remain in a meta-stable state and only those are triggered were a thermal electron reaches the conductive band. G-MAPD's achieve a very high gain (in the range of 10^5 to 10^7). Due to their excellent single photon resolution G-MAPD's are sometimes also called silicon-photo-multipliers (SiPM).

In this chapter the working principle of the above mentioned photon-detectors are explained. The main emphasis is put on the working principle of G-MAPD's, their pulse-height spectrum and on two of their possible structures (surface-resistor and micro-well). As a reference work on solid state photon detectors a publication of D.Renker and E.Lorenz [1] was used.

Photodetector type	Minimal detectable signal
Silicon PIN photodiodes	200-300 p.e. [1]
Silicon APD	10-20 p.e. [1]
Silicon VLPC	1 p.e. [1]
Silicon G-MAPD	1 p.e. [1]
PMT	1 p.e.

Table 1.1: Photon detecting efficiency of different photodetector types.

1.1 The photomultiplier tube

The photomultiplier tube (PMT) is a special vacuum tube to detect photons of low flux. It's structure consists basically of three parts housed in a vacuum tube: a photocathode, a dynode chain and an anode (see figure 1.1).

A photon reaching the PMT's photocathode hits an electron out of the cathodes surface (outer photo effect). The released photo-electron is then accelerated in an electric field towards the first dynode. There it knocks out secondary electrons and undergoes multiplication (by a factor in the range of 3 to 10 depending on the type of the PMT). Each following dynode is at a lower electrical potential providing an electric field that forces the electrons to snowball to the anode (at ground potential). This leads to gains in the range of 10^4 to 10^7 .

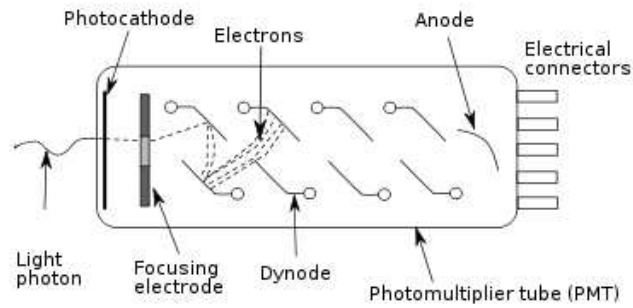


Figure 1.1: Schematic view of a photo-multiplier-tube.

The potential on the dynodes is usually achieved with a voltage-divider outside the PMT (see figure 1.2). It divides the supply voltage applied to the PMT. The electrons are finally collected at the anode and flow over a resistor to the ground. Over this resistor a voltage pulse arises depending on the number of original photo-electrons.



Figure 1.2: Simple voltage-divider soldered directly on to the electrical connectors of a PMT (the Hamamatsu R7725 MOD used in the small LAr TPC experiment at LHEP Bern).

Depending on the field where the PMTs are used the desired properties vary over a wide range (e.g. size, spectral range, gain, environment temperature, pulse rise time, etc.). Today hundreds of PMTs from different manufacturers (e.g Hamamatsu, Philips, etc.) are commercially available to meet the very specific requirements. Figure 1.2 shows three PMTs used in the LAr TPC projects at LHEP Bern.



Figure 1.3: Three PMTs of different size next to a 20 cm long ruler: the Hamamatsu R5912-02MOD used in the medium LAr TPC experiment at LHEP Bern (left), the Philips 53AVP which is similar in size to the Hamamatsu R7725 MOD (middle), the Hamamatsu R1450 used for some test runs in the small LAr TPC (right).

The PMT is a very successful and highly developed device. It has however some weak points:

- It does not work in magnetic fields or has to be well shielded
- High voltage (depending on size and model in the range of some hundred to few kV) is needed to supply the PMT
- It is fragile due to the glass used
- Some PMTs do not tolerate accidental illumination
- They are relatively large

1.2 Semiconductor photon detectors

The p-n-junction The essential building block for almost all semiconductor devices is the p-n-junction. It was discovered by chance in the early 40's at the Bell Telephone Labs by Russell Shoemaker Ohl [2], who was investigating the use of silicon crystals in radar detectors. He noticed that one of his purest silicon crystals behaved differently from the others. When exposed to bright light the current flowing through

it jumped noticeably. He examined the crystal and found that it had a crack due to different impurities (doping) on each side.

On one side of the crack the Silicon had depositions of Phosphor on the other side of Boron. Phosphor added extra electrons (it acted as a so-called donor) while Boron wanted to bind these electrons (acting as a so-called acceptor). The region with the donor, where electrons are the free charge carriers, is called n-type (negative). The region with the acceptor, where positive charged holes are the free charge carriers, is called p-type (positive). If the two differently doped silicon types get in connection with each other, like at the crack in Ohl's silicon crystal, they generate a junction (the so-called p-n-junction, see figure 1.4).

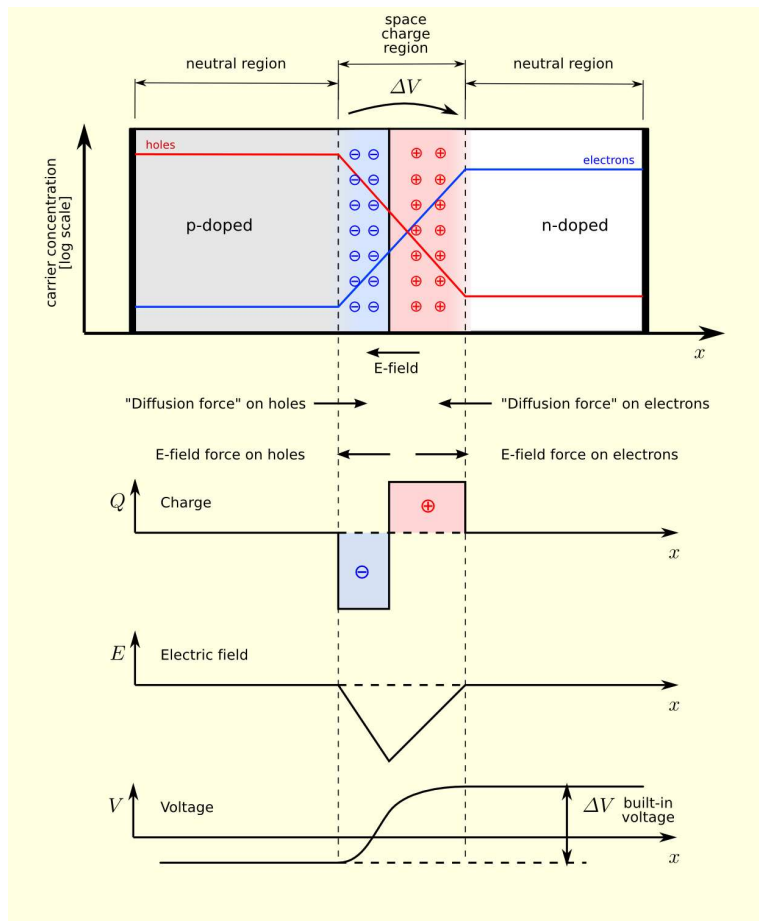


Figure 1.4: Schematic of a p-n-junction (modification of [3]).

At this junction the free charge carriers of both types start to diffuse into the opposite region. This charges up the region around the junction (the so called space-charge-region) and an electric field is generated. This field acts on the charge carriers in the opposite direction as the diffusion-force. An equilibrium state is reached when the two forces balance each other out. The mixed charge carriers around the junction

recombine, depleting the space-charge-region (thus sometimes also called depletion-layer).

The result of the process elucidated before is a layer around the p-n-junction with almost no charge carriers (depletion-layer) and an intrinsic electric potential across. An external voltage applied (e.g by a battery) over the p-n-junction is called bias-voltage. If the positive pole of the battery is connected to the p-type silicon and the negative to the n-type, the p-n-junction is forward-biased. The potential of the battery is opposite to the intrinsic potential thus the diffusion of the free charge carriers over the junction is supported. The holes and electrons added from the battery recombine at the junction and are being replaced by new ones out of the battery. A current flows through the forward-biased p-n-junction [4]:

$$J(V_{forward}) = J_0 \exp(e|V|/k_B T) \quad (1.1)$$

The Boltzmann-factor gives the amount of electrons with enough energy to overcome the potential barrier at the junction. If the battery is connected the other way around, the p-n-junction is reversed-biased. The intrinsic potential and the potential from the battery are aligned and thus the diffusion is suppressed. The added electrons recombine with the holes of the p-doped silicon and vice versa on the other side of the junction [4]:

$$J(V_{reversed}) = J_0 \exp(-e|V|/k_B T) \quad (1.2)$$

Figure 1.5 shows the current-voltage diagram of a p-n-junction which is well described (except the effect of breakdown) by the formula for the total current [4]:

$$I(V) = I_0(\exp(eV/k_B T) - 1) \quad (1.3)$$

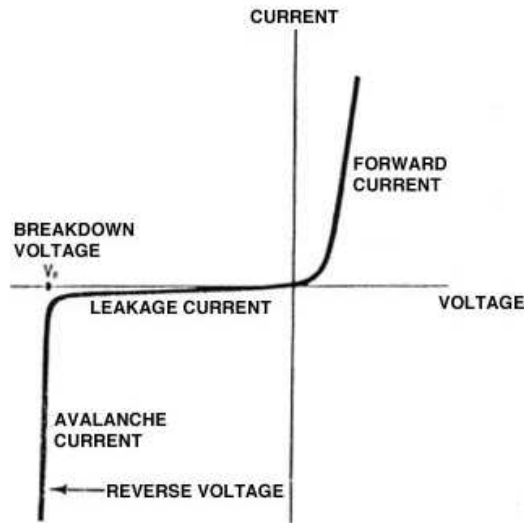


Figure 1.5: Current-voltage-diagram of a p-n-junction [5].

Photons absorbed in the depletion region of the p-n-junction generate a electron-hole pair by lifting the electron over the band-gap, from the valence-band to the conductive-band. The two generated charge-carriers drift in the intrinsic field towards the poles and a small current arises. If enough photons get absorbed in a short time this current can be measured and the p-n-junction can be used as a photon-detector. However due to the properties of the p-n-junction one of its first applications were diodes used in rectifiers. The p-n-junction is as well the basis of today's semiconductor technology.

Photon absorption in silicon The absorption length of photons in silicon is wavelength dependant. If the photon has less than 1.12 eV it can only be absorbed by free electrons who are rare in semiconductor and thus the absorption-length is rather large. Photons with more than 1.12 eV can lift an electron over the band-gap and get absorbed. In this process a phonon is needed for momentum conservation. To absorb a photon with energy close to 1.12 eV a phonon with high momentum is needed. With increasing energy of the photon the absorption requires less momentum from the phonon. Low momentum phonons occur more frequent and thus the absorption length gets shorter. Photons with energies above 3.4 eV (wavelength ≈ 350 nm) can undergo a direct transition leading to a even shorter absorption-length (fig. 1.6).

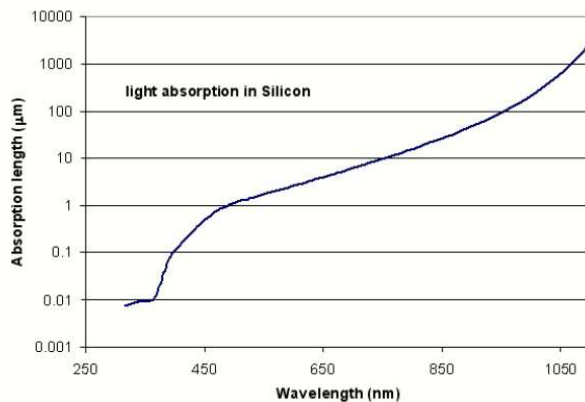


Figure 1.6: The absorption-length of photons in silicon depending on their wavelength [6].

The p-i-n-photodiode The positive-intrinsic-negative-photodiode (PIN) is basically a p-n-diode with a intrinsic silicon-layer potted between the heavily doped positive and negative layers (fig. 1.7). The intrinsic-layer has only a few free charge-carriers and is thus high-ohmic. Even without a applied bias voltage this structure maintains an electric potential, which separates charges produced in the depletion-region. These charges drift to the border of the depletion-region and are detected as a current. The thick ($300 \mu\text{m}$) intrinsic-layer makes the device sensitive to light with

long absorption-length (e.g. red and infra-red, see fig. 1.6). Because the intrinsic-layer is poorly doped, only a small applied bias voltage is needed to deplete it completely.

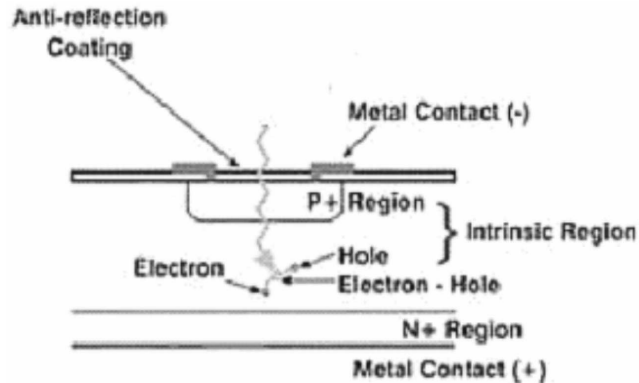


Figure 1.7: Structure of a PIN-diode [1].

The PIN photodiode was the first solid-state-photodiode used in particle physics experiments to detect photons of low flux (few hundred photons within less than a few μsec [1]). In contrast to the PMTs, the PIN photodiode works still very well under the influence of high magnetic-fields, used in most particle-detectors to identify charged particles. Their quantum-efficiency (QE) goes up to over 80% at a wave length of 550 nm [1], where PMTs are in the range of 10-15%. PIN photodiodes have however no internal gain and the minimum detectable signal is in the range of several hundred photons (tab. 1.1).

The avalanche photo-diode The avalanche photo-diode (APD) is basically a reverse biased p-n-junction. Over the junction a high electric field is generated due to the bias voltage. The charge-carriers (electron-hole pairs) produced by photons in the depletion-region undergo acceleration. If the electric field is high enough (above the ionization threshold for electrons in silicon: $1.75 \cdot 10^5$ V/cm [7]), the electrons gain enough energy to produce other electron-hole pairs through impact ionization. Thus an avalanche in the depletion region occurs. If the electric field is not too high (below the ionization threshold for holes in silicon: $2.5 \cdot 10^5$ V/cm [8]) only the electrons, which have higher mobility than the holes, gain enough energy to ionize. Thus the avalanche evolves only in one direction and stops as soon as all the produced electrons have reached the border of the depletion-region. This mechanism leads to a internal gain of the APD. If also the holes start ionization the avalanche gets out of control and break-down occurs. The standard APDs have to be operated far below the ionization threshold for holes, otherwise the gain stability gets lost and spontaneous breakdown may occur. Thus with standard APDs a moderate gain in the range of 50 to 200 can be achieved. There are mainly three different APD structures used, the bevelled-edge, the reach-through and the reversed or shallow junction APD. The

figure 1.8 shows the p-on-n structure of these APD's, they are peak sensitive to blue light. If the dopants are swapped and a n-on-p structure with peak sensitivity for red light is achieved. The bevelled-edge and the reach-through structure maintain a high multiplication deep into their structures. The shallow junction APD however has only a short multiplication region and is thus only sensitive to light with very short absorption-length (e.g. blue).

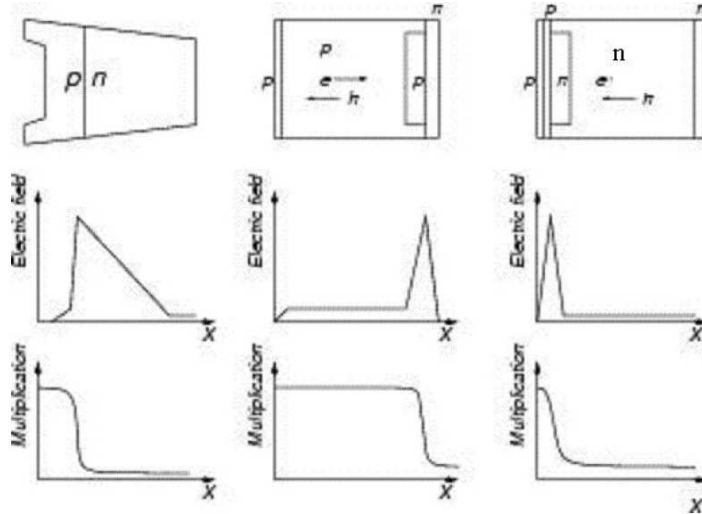


Figure 1.8: Structures, electric field and electron/hole multiplication for (left) bevelled-edge, (middle) reach-through and (right) shallow junction APDs (modified from [9]).

The visual-light-photon-counter (VLPC) works at electric fields very close to the ionization threshold for holes. Thus much larger gains can be achieved. To operate it stably in this high field region the temperature of the VLPC has to be very low (6 to 8 Kelvin) and well stabilized. The only experiment ever used VLPCs in large quantity's is the $D\bar{O}$ experiment at Fermilab, USA.

The Geiger-mode avalanche photo-diode The Geiger-mode avalanche photo-diode (G-APD) works with a bias voltage above the breakdown voltage (above the ionization threshold for holes). In this region both, electrons and holes, gain enough energy to produce new electron-hole pairs by impact ionization. The avalanche generated evolves in both directions and is self sustaining, break-down occurs. To quench the avalanche the electric-field has to be decreased below the critical value of hole ionization. Usually this is done by putting a high ohmic resistor in series with the bias-voltage-supply. Thus if the G-APD is triggered the voltage over it will drop and quench the avalanche. After a while the voltage over the G-APD is recovered and it is again ready for triggering. With this mechanism a very high gain proportional to the over voltage can be reached:

$$A = C/q \cdot (V_{bias} - V_{breakdown}) \quad (1.4)$$

Where A is the amplification (or gain), C the capacity of the G-APD, q the electron charge and $V_{bias} - V_{breakdown}$ the over-voltage. However the G-APD is in a finicky meta-stable state, where a single electron-hole-pair or a free thermal electron is enough to trigger the breakdown. Thus only very small volumes, where the probability of a thermal free electron is small, can be kept biased over the breakdown voltage for a long enough time. As a logic consequent a structure with many small pixels, each acting like a G-APD, is used in the so-called Geiger-mode micro-pixel-APD (G-MAPD).

The Geiger-mode micro-pixel avalanche photo-diode If in the G-MAPD a pixel gets triggered by either a photon or a thermal electron only this pixel will breakdown and leave the others unaffected. This is however the ideal case and in reality cross-talk between neighbouring pixels may occur. I.e. photons rarely created in an avalanche may be absorbed in a neighbouring pixel and triggering it (optical cross-talk) or an avalanche could evolve over the border of its pixel and as well trigger neighbouring pixels (electric cross-talk).

Also if the pixels are very small, thermal electrons still occur very frequently. This leads to a high noise-rate (around 100 kHz) in the range of a single p.e.-response of the G-MAPD. The noise-rate decreases however rapidly for a larger threshold and goes below 1 Hz for a 3-p.e.-response. Despite the high noise-rate the majority of the micro-pixels are in the meta-stable-state ready for triggering.

To quench the avalanches in the triggered micro-pixels, generally G-MAPD's are constructed with individual surface resistors for each pixel (fig. 1.9). An alternative structure is the micro-well structure, which allows a very high cell density. This structure is only produced by Z. Sadygov, Dubna and Zecotek¹. Worth mentioning is the fact that this structure does not need any surface resistors. In this structure the avalanche is quenched by charge accumulated at the micro well. This reduces the electric field in the avalanche region and thus stops it. The micro-pixels recover much faster with this structure because the top-layer does not need to be as high ohmic as with the surface-resistor structure.

G-MAPDs with surface-resistor structures fail in cryogenic environments, because the properties of the surface-resistor change with temperature. The micro-well structured G-MAPD do not have this limitation. For the first time such a G-MAPD (the Zecotec "MAPD-3N") has been characterized at cryogenic environments in the framework of this thesis. It was found that this structure works very well under these conditions.

¹www.zecotek.com

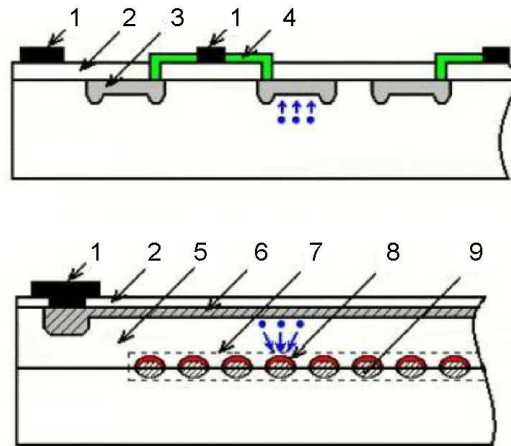


Figure 1.9: Schematic views of the surface-resistor (top) and the micro-well structure of G-MAPD's: 1- common metal electrode, 2- buffer layer of silicon oxide, 3- p-n-junctions/micro-pixels, 4- individual surface resistors, 5- epitaxial silicon layer of p-type conductivity, 6- a high-doped silicon layer of p-type conductivity, 7- a region with micro-wells, 8- local avalanche regions, 9- individual micro-wells. (Modified from [1] which is a reprint from [10]).

G-MAPD's have a very high sensitivity and large internal gain (in the range of 10^5 to 10^7). The single photon resolution achievable with G-MAPD is almost as good as with the best PMT's (fig 1.10).

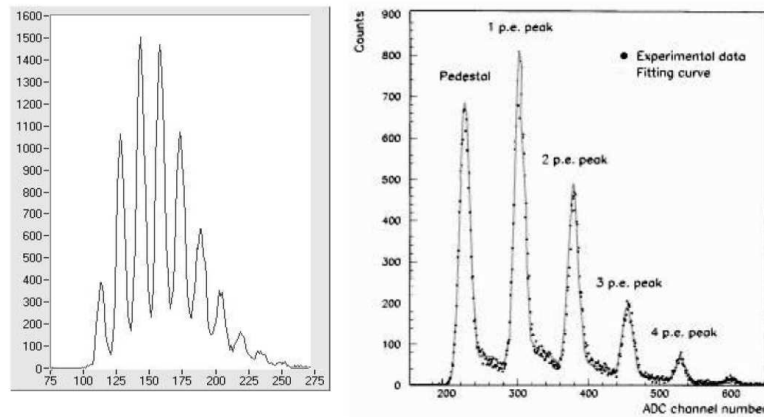


Figure 1.10: The pulse-height-spectrum of low intensity light pulse recorded with a G-MAPD Hamamatsu 1-53-1A-1 (left, modified [1]) and a PMT [11]. All axes in arbitrary units.

The output signal of a G-MAPD is proportional to the number of cells fired. Each cell works like a simple G-APD and has itself a standard response, depending on the over-voltage and its capacity (eq. 1.4). This leads to the characteristic shape of the G-MAPD pulse-height-spectrum (as seen in figure 1.10). Due to small differences in the cells capacities and inhomogeneity of the electric field, the cells response is not perfectly standardised. It is Gaussian spread (eq. 1.5) around a mean-value given by the equation (1.4), $\mu_0 = A$.

$$g(x, \mu_0, \sigma) = \frac{1}{\sigma\sqrt{2} \cdot \pi} \cdot \exp\left(-\frac{1}{2} \left(\frac{x - \mu_0}{\sigma}\right)^2\right) \quad (1.5)$$

If two or more cells are fired at the same time, the output signal of the G-MAPD is just the sum of their standard pulses. This signal is again Gaussian spread with a mean-value of $\mu_k = k \cdot \mu_0$, where k is the number of cells fired. The standard deviation increases by a factor \sqrt{k} :

$$g_k(x) = g(x, k \cdot \mu_0, \sqrt{k} \cdot \sigma_0) \quad (1.6)$$

The probability of firing k cells at the same time is Poisson distributed:

$$P(p.e. = k) = \frac{\lambda^k}{k!} \cdot \exp(-\lambda) \quad (1.7)$$

This leads to a simplified formula describing the pulse-height-spectrum of a G-MAPD (fig. 1.11):

$$f(x) = \sum_{k=0}^n \cdot P(k) \cdot g(x, a \cdot k, \sqrt{k} \cdot \sigma_0) \quad (1.8)$$

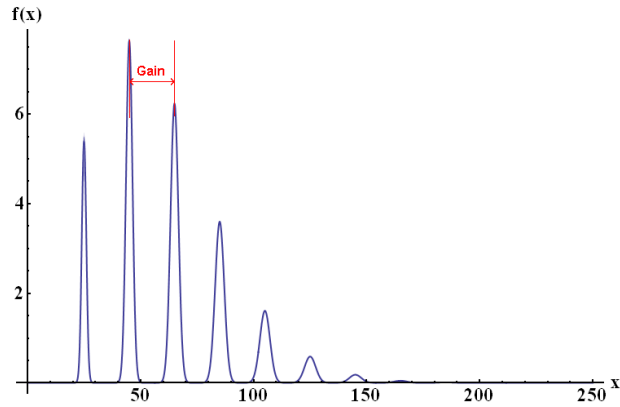


Figure 1.11: Plot of the function describing the characteristic pulse-height-spectrum of a G-MAPD. The gain is indicated in red.

Chapter 2

Experimental set-up, data taking and processing

The G-MAPD "MAPD-3N" manufactured by Zecotek in Russia has been immersed in liquid Nitrogen (77 K) and liquid Argon (87 K). The pulse-height spectrum and the noise-rate spectrum of the G-MAPD has then been measured at several bias voltages covering most of the working range. From the pulse-height spectrum, the gain and cross-talk were estimated (see Section 2.3). To do so an experimental set-up was designed with the possibility of keeping the G-MAPD at constant cryogenic temperature. To reduce the pick-up noise and thus increase the resolution of the readout signal a pre-amplifier (the "AMP_0604" manufactured by Photonics SA in Geneva, Switzerland) was used (see figure 2.1).

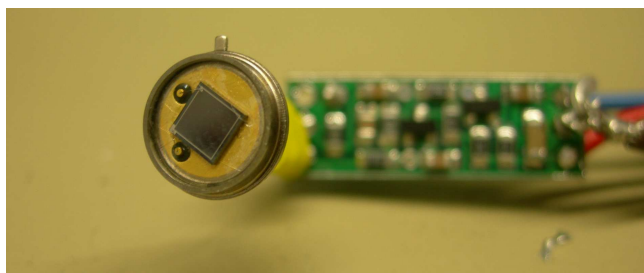


Figure 2.1: The "AMP_0604" (Photonics SA) with the "MAPD-3N" (Zecotek) mounted.

2.1 Set-up

Because the G-MAPD is highly sensitive to light all the measurements needed to be done in the absence of disturbing light. A light tight box with a filling system for the cryogenic liquids was constructed. A tank for these liquids was installed above the box. Through an insulated copper tube the liquids flow from the tank into the box where the automatic level regulating valve controlled the flow. To keep

the temperature of the G-MAPD stable it was completely immersed in the cryogenic liquid. Outside the box the pre-amplifier was mounted and kept at room temperature with the help of a fan and a heat-exchanger. To measure the pulse-height spectrum of the G-MAPD the light of a LED was led through a light guide into the box close to the G-MAPD. Figure 2.2 shows the experimental set-up and figure 2.3 shows a close view on the box. The automatic level control valve was specially designed and constructed for its use in this box (see Appendix A).

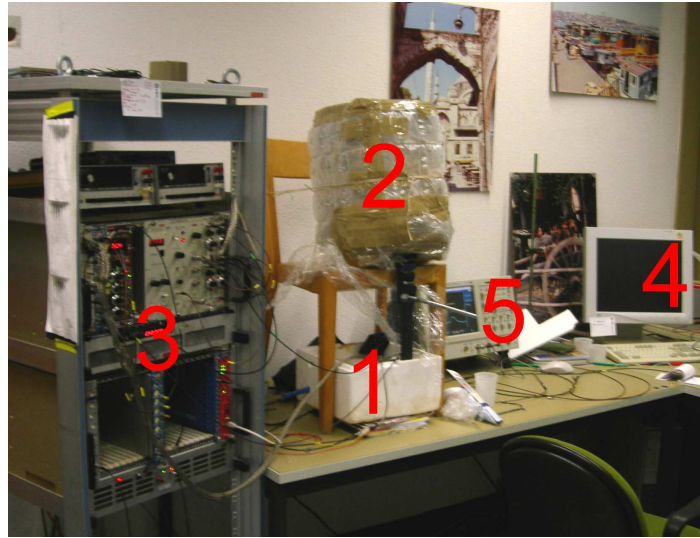


Figure 2.2: Photo of the experimental set-up: 1- box with G-MAPD inside, 2- insulated tank for the cryogenic liquids, 3- electronics for light pulse generation and signal readout, 4- PC for data acquisition (DAQ), 5- oscilloscope used as a monitoring device.



Figure 2.3: Photo of the open box (left) and the cover (right): 1- G-MAPD with shielding , 2- pre-amplifier wrapped in a shielding in thermal contact with a heat-exchanger, 3- light conductor , 4- automatic level control valve inside the bath for the cryogenic liquids.

2.2 Measuring procedures

Measuring the pulse-height spectrum To measure the pulse-height spectrum of the G-MAPD a fixed bias voltage was set at the according power-supply (Ortec: 710 Quad Bias Supply). With two dual-timer-units (Uni Bern: N2255) a cycle was realised which triggered the LED-generator (Uni Bern: UB/G11) and a few nanoseconds later the gate (≈ 40 ns) of the integrator (LeCroy: 2249W ADC). Then it paused ($>1 \mu s$) before it restarted. Triggering the LED-generator forced the LED to emit a short light pulse (≈ 1 ns) of only a few photons. To reduce the pick-up noise caused by the voltage pulse of the LED-generator on to the G-MAPD a light conductor was used. The light conductor allowed to increase the distance between the LED and the G-MAPD and thus to reduce the pick-up noise.

The response of the G-MAPD to the light pulse was a small current pulse (see figure 2.4) which was immediately amplified with the pre-amplifier. The Signal was amplified a second time (Uni Bern: UBA5) and integrated. Then the integrated signal was read out with the PC. A link-card (C.E.A.N.: Mod.C111C) was used to connect the ADC with the PC via Ethernet. Figure 2.5 shows a schematic of the signal process used for the measurements of the G-MAPD spectra and in figure 2.6 a photo of the racks used for the signal processing is shown.

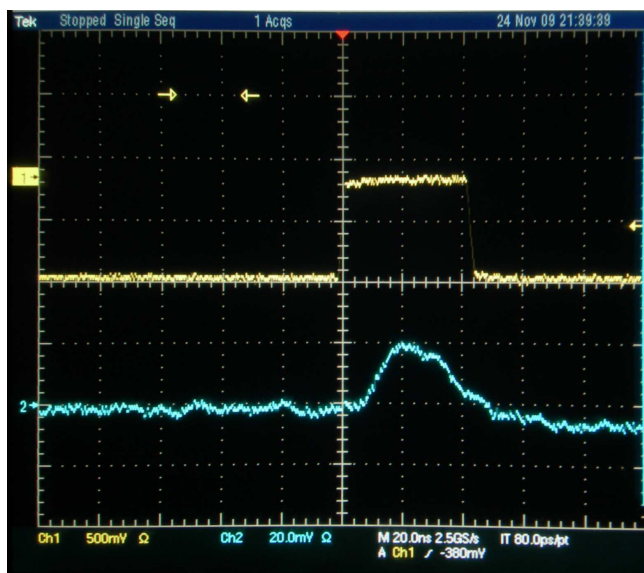


Figure 2.4: Picture of the oscilloscope screen: blue- signal of the G-MAPD after full amplification, yellow- gate for the integrator.

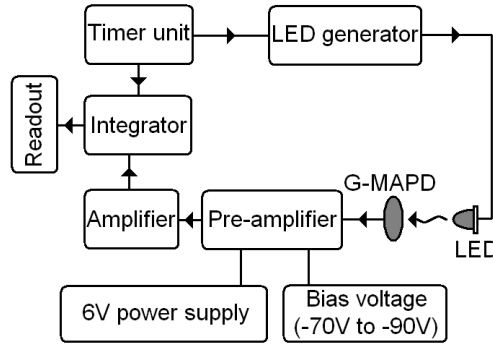


Figure 2.5: Schematic of the data flow used for pulse-height spectrum measurements.

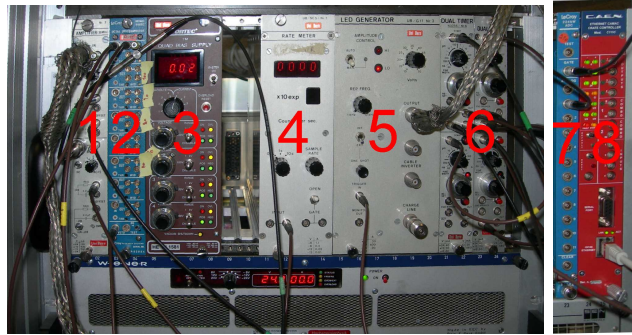


Figure 2.6: Photo of the NIM-rack (left) and CAMAC-rack: 1- amplifier , 2- discriminator , 3- HV-supply for bias-voltage , 4- rate-meter , 5- LED-generator , 6- dual-timer , 7- ADC integrator card , 8- link card.

Measuring the noise-rate spectrum To measure the noise-rate spectrum some small changes had to be done. No light pulse was needed and therefore the LED was plugged off. To have a threshold a discriminator (LeCroy: 4608C) was used. The gate of the integrator was only opened if the signal was larger than the minimal threshold set at the discriminator. For the noise-rate spectrum measurement the gate of the integrator had to be wider (≈ 60 ns) than for the pulse-height spectrum measurements. Because the shape of the signal varied and thus the stability of the gate with respect to the signal was less. To measure the full rate a rate-meter (Uni Bern: UB/Sc5a) was connected to the discriminator output. Figure 2.7 shows a schematic of the signal process used for the noise-rate spectrum measurement.

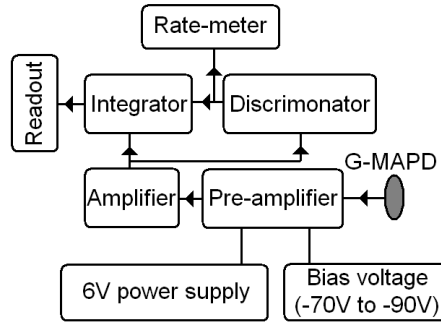


Figure 2.7: Schematic of the data flow used for noise-rate spectrum measurements.

Calibration To calibrate the ADC-channels again some changes had to be done. A signal-generator (Agilent 33250A) was used to generate a square pulse which was connected to the G-MAPD via a capacitor (fig. 2.8). This led to a well defined charge injection into the circuit. The gate (≈ 40 ns) of the integrator was triggered directly from the signal-generator (fig. 2.9). The calibration was done at room temperature with the bias voltage (-80V) set a few volts below the working-point of the G-MAPD.

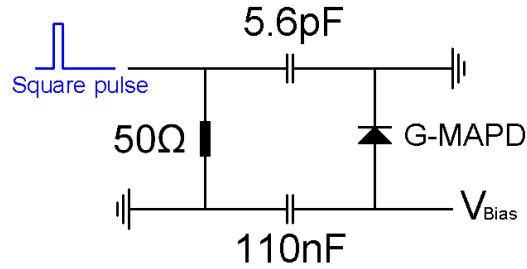


Figure 2.8: Diagram of the circuit used to inject the charge.

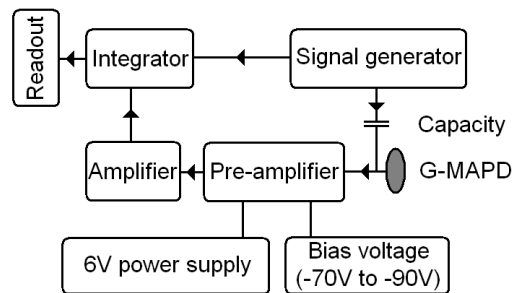


Figure 2.9: Schematic of the data flow used for calibration.

2.3 Data processing

Calibration of the ADC channels The data read out by the computer was saved in histograms. The x-axes were in arbitrary units and a calibration factor, to scale the x-axes, had to be calculated. Figure 2.10 shows an example of a pulse-height spectrum and noise-rate spectrum in arbitrary units.

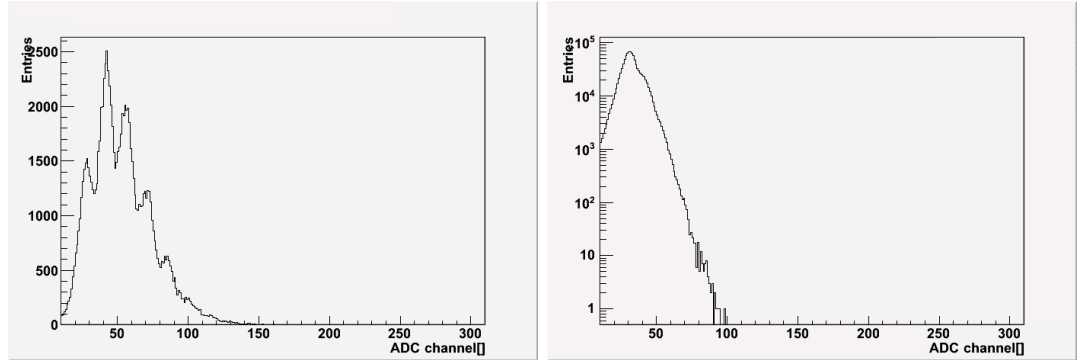


Figure 2.10: Examples of a pulse-height (left) and noise-rate spectrum (right) before post-processing.

To calibrate the ADC channels a calibration curve had to be measured. As explained in the previous section a voltage pulse was used to inject charge over a capacity into the circuit (fig. 2.8). At three different amplitudes of this voltage pulse the response of the circuit was measured (fig 2.11).

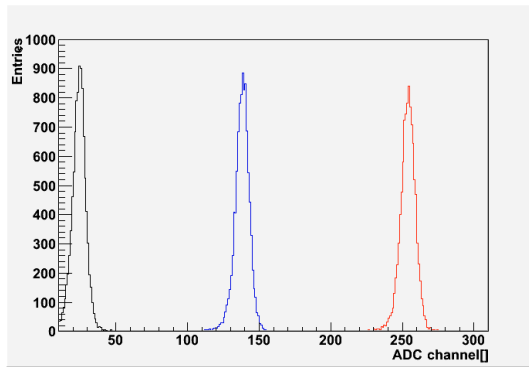


Figure 2.11: Response of the circuit to the injected charge: -black at 0 mV amplitude, blue- at 15 mV, red- at 30 mV.

To estimate the mean values of the three peaks shown in figure 2.11 each of them was fitted with a Gaussian. Out of the fit-parameters the mean values and their errors were determined. Figure 2.12 shows these mean values versus the amplitude of the voltage pulse.

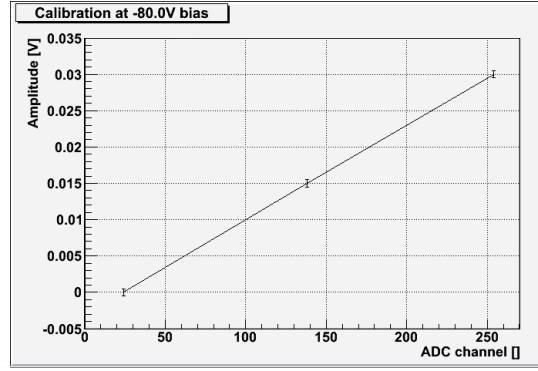


Figure 2.12: Mean values of the response of the circuit to the injected charges (the errors of the mean values are very small can not be seen here).

The charge injected can be calculated from of the amplitude of the voltage pulse by the simple relation:

$$Q = C \cdot U \quad (2.1)$$

With its error:

$$\Delta Q = \sqrt{C^2 \cdot \Delta U^2 + U^2 \cdot \Delta C^2} \quad (2.2)$$

Where Q is the injected charge, C the capacity used ($5.6 \text{ pF} \pm 5\%$) and U the amplitude of the voltage pulse (error: $\pm 0.5 \text{ mV}$). In figure 2.13 the before mentioned mean values versus the injected charge are shown.

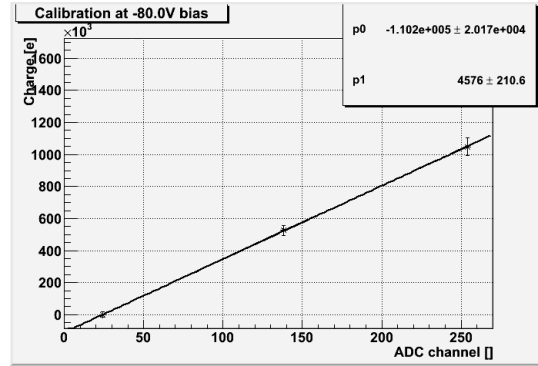


Figure 2.13: Calibration curve, mean values of the circuits response versus the injected charges (in units of e , the electron charge).

A linear fit was made in figure 2.13 to get the final calibration factor:

$$1 \text{ ADC channel} = 4576 \pm 210.6e = 4676e \pm 4.6\% \quad (2.3)$$

Figure 2.14 shows the previous pulse-height spectrum after scaling the x-axis.

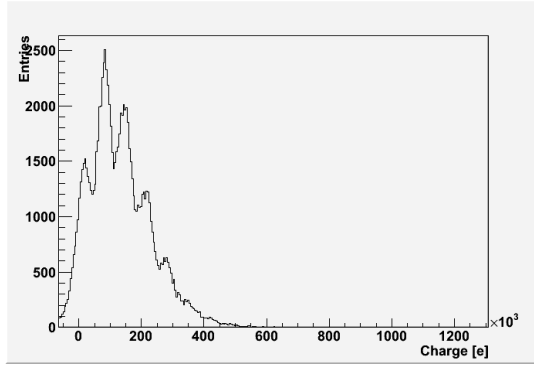


Figure 2.14: Pulse-height spectrum after scaling the x-axis.

Determination of the gain The gain of the G-MAPD can be obtained out of its scaled pulse-height spectrum (fig 1.11). The function 1.8 needs however to be extended to include the electric noise. It has to be convoluted with a Gaussian of the width σ_e , representing the electric noise. Each of the peaks is already described with a Gaussian of width σ_k . The convolution leaves these Gaussians invariant and changes only their width:

$$\Sigma_k = \sqrt{\sigma_k^2 + \sigma_e^2} \quad (2.4)$$

Thus the function describing the measured pulse-height spectrum becomes:

$$f(x) = \sum_{k=0}^n \cdot P(k) \cdot g(x, a \cdot k, \Sigma_k) \quad (2.5)$$

This function was used to fit the pulse-height spectrum, where the fit-parameter "a" represents the gain (fig. 2.15).

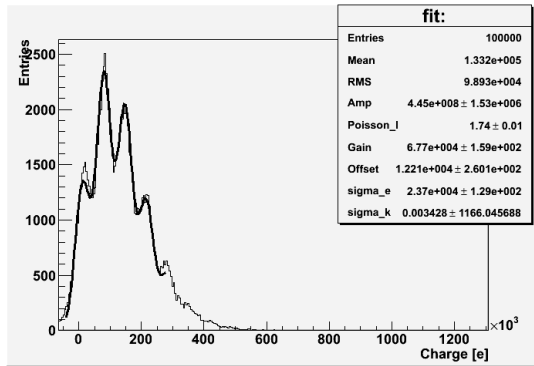


Figure 2.15: Pulse-height-spectrum with the function $f(x)$ fitted to the measured curve.

This procedure was done with each spectrum measured, to derive the gain of the G-MAPD at different bias voltages and temperatures. Figure 2.16 shows four pulse-height spectra taken at 87 K (liquid Argon) with different bias voltages applied.

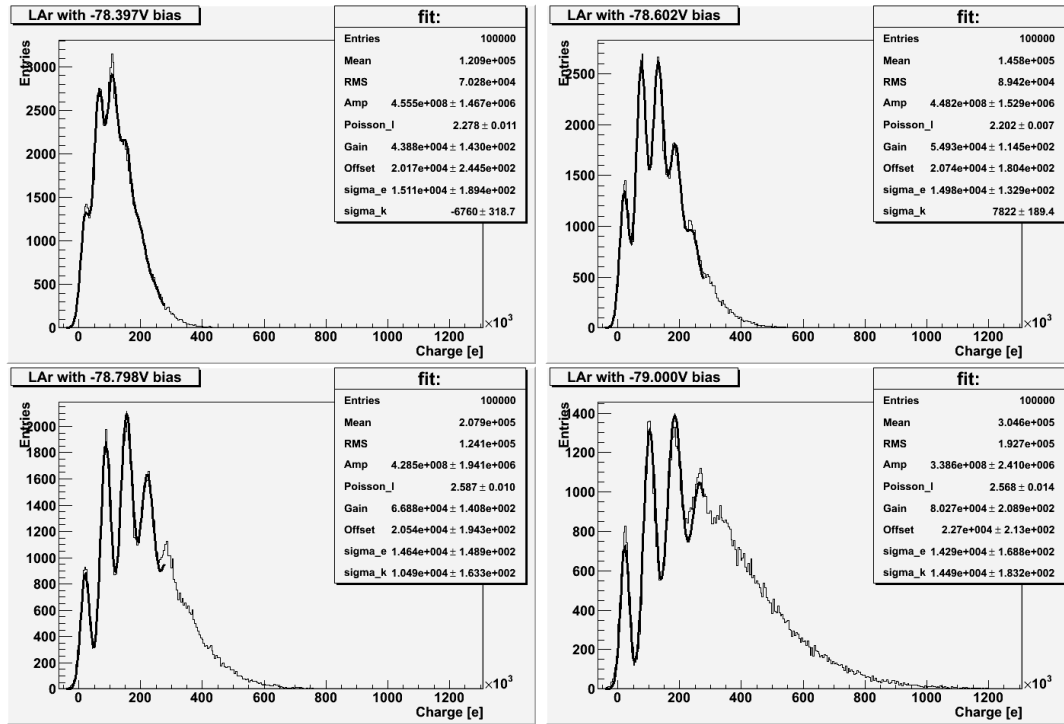


Figure 2.16: Pulse-height-spectrum measured at 87 K with different bias voltages: -78.397 V, -78.602 V, -78.798 V, -79.000 V (left to right, top to bottom).

In Figure 2.17 the gain of the G-MAPD versus the applied bias voltage is shown for three temperatures.

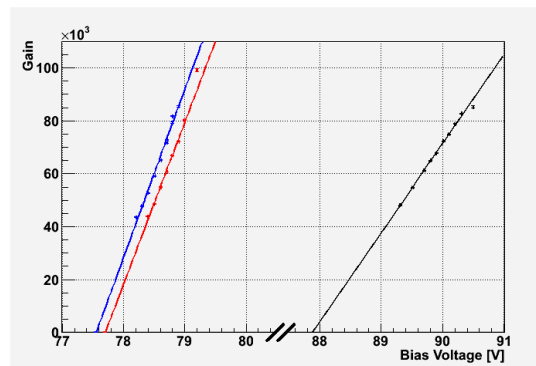


Figure 2.17: Gain versus bias-voltage for three temperatures: blue- 77 K, red- 87 K, black- 298 K.

Each of these gain-curves was fitted linearly. Out of these fits the break-down-voltage (by extrapolating the fit to zero gain) and the slope of the gain dG/dV_{bias} were estimated (fig. 2.18). The slope of the gain is proportional to the diode capacity 1.4.

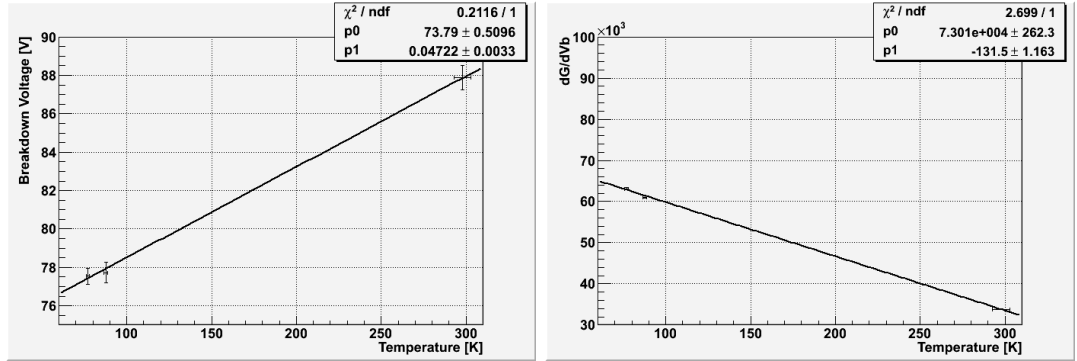


Figure 2.18: Breakdown voltage (left) and slope of the gain (right) versus temperature.

Estimation of the cross-talk As seen in figure 2.16, at higher bias voltage (e.g. higher gain) the right tail of the pulse-height spectrum starts to blur out. This effect is due to cross-talk (also called X-talk). In this thesis only an estimation and no absolute measurement of the cross-talk was done. The method used to estimate the cross-talk is based on the Poisson distribution of the number of photons hitting the G-MAPD. Two ways to determine the parameter λ of the Poisson distribution 2.6 were used for each pulse-height spectrum. The ratio of these two λ 's is considered to be the cross-talk factor (or X-factor).

$$P(X = k) = \frac{\lambda^k}{k!} \cdot \exp(-\lambda) \quad (2.6)$$

With the first method λ_1 was determined over the probability of an entry in the pulse-height spectrum being a pedestal entry:

$$P(p.e. = 0) = \frac{\lambda_1^0}{0!} \cdot \exp(-\lambda_1) = \exp(-\lambda_1) \quad (2.7)$$

and thus:

$$\lambda_1 = -\ln(P(p.e. = 0)) \quad (2.8)$$

The probability $P(p.e. = 0)$ is given by the ratio of the number of pedestal entries to the number of total entries. To derive the number of pedestal entries in a pulse-height spectrum, a normalized Gaussian 2.9, multiplied with factor "N", was fitted to the pedestal peak (fig. 2.19). The factor "N" is the integral of the normalized Gaussian and thus the number of pedestal entries.

$$g(x) = N \cdot \frac{1}{\sigma\sqrt{2 \cdot \pi}} \cdot \exp\left(-\frac{1}{2} \left(\frac{x - \mu}{\sigma}\right)^2\right) \quad (2.9)$$

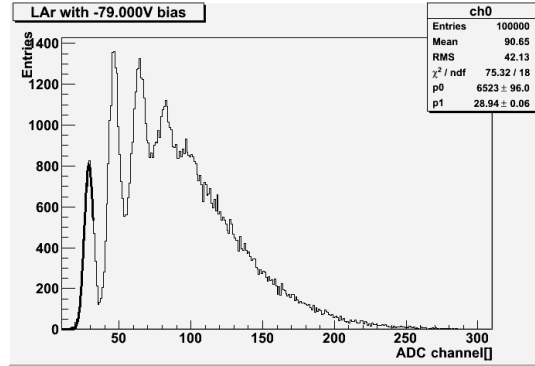


Figure 2.19: A Gaussian fitted to the pedestal peak of a pulse-height spectrum (with p_0 the number of pedestal entries and the mean value of the total spectrum).

The total number of entries in a pulse-height spectrum can be derived directly from the data-file used (or by integrating over the whole spectrum). The second method to derive λ_2 uses the fact that the expectation value (or synonymic the mean value) of a Poisson distribution is λ_2 itself:

$$E(X) = \lambda_2 \quad (2.10)$$

The mean-value can also be derived directly from the pulse-height spectrum (fig. 2.19). The ratio λ_1/λ_2 is considered to be the cross-talk factor (fig. 2.20). This method is justified by the fact that the cross-talk has no influence on the pedestal (i.e. λ_2), but on the other peaks in the pulse-height spectrum, who are due to cells fired, and thus on the mean-value (i.e. λ_1).

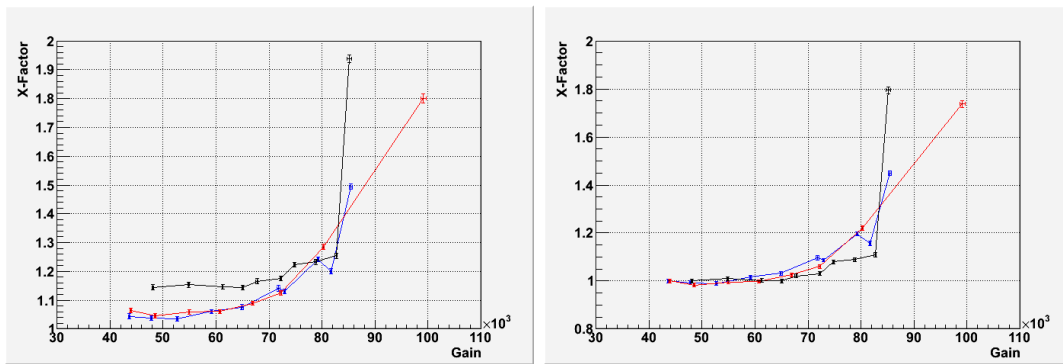


Figure 2.20: Cross-talk factor versus gain: blue- 77 K, red- 87 K, black- 298 K. On the right side for better clarity normalized to one.

Determination of the noise-rate To determine the noise-rate $F(x)$ above a certain threshold the noise-rate spectrum $f(x)$ was integrated (fig. 2.21):

$$F(x) = f(x > threshold) = \int_{threshold}^{\infty} f(x)\delta x \quad (2.11)$$

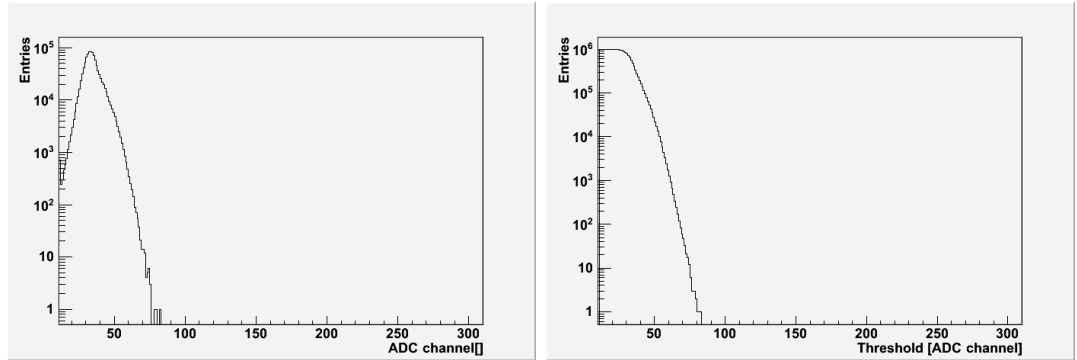


Figure 2.21: Noise-rate spectrum (left) and integrated (right). Measured at 298 K with -89.5 V bias voltage applied.

After the integration both axes were scaled. The calibration factor and the gain, at the respective bias voltage, were used to scale the x-axis to units of photo-electrons (p.e.). To scale the y-axis, the full noise-rate (measured with the rate-meter) was used. Figure 2.22 shows three such curves, measured at different temperatures but approximately the same gain.

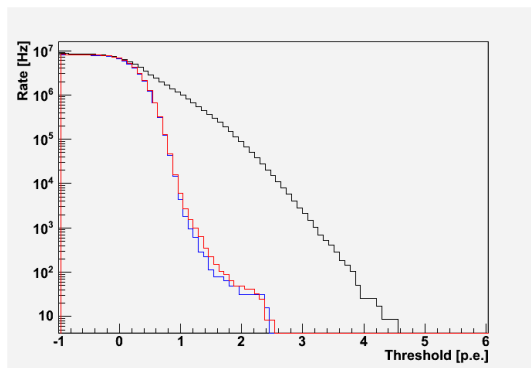


Figure 2.22: Noise-rate versus threshold at a gain of approximately $5.5 \cdot 10^4$: blue- 77 K, red- 87 K, black- 298 K.

2.4 Specifications of the "MAPD-3N" at cryogenic conditions

The gain dependence on the bias voltage of the G-MAPD "MAPD-3N" manufactured by Zecotek in Russia was measured at three temperatures. The results (fig. 2.23) show that this dependence is linear. This is consistent with the theoretical prediction (eq. 1.4). Almost independent of the temperature a gain in the range of $5 \cdot 10^4$ to 10^5 can be reached. This gain is smaller than the gain of standard G-MAPDs. This is however explained by the fact that the micro-pixels of the "MAPD-3N" are much smaller, and thus have a smaller capacity, than the cells of standard (surface-resistor type) G-MAPDs. The advantage of this small micro-pixel is its large density ($40'000$ pixels per 1 mm^2) and thus high dynamic-range.

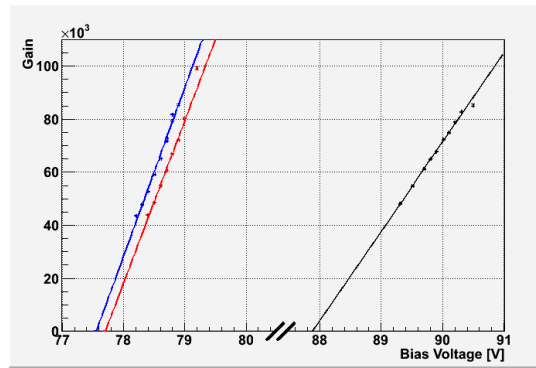


Figure 2.23: Gain versus bias voltage for three temperatures: blue- 77 K, red- 87 K, black- 298 K.

The breakdown voltage of the "MAPD-3N" increases with the temperature while the slope of the gain, and thus the diodes capacity, decreases (fig. 2.24). These two effects are not completely understood by the candidate.

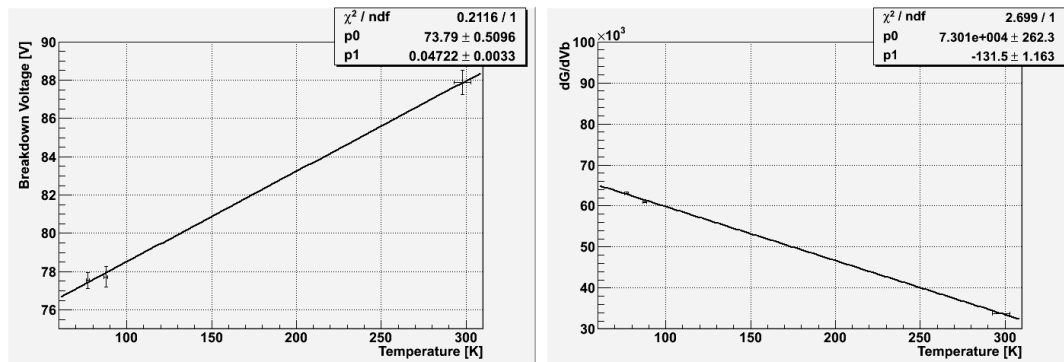


Figure 2.24: Breakdown voltage (left) and slope of the gain (right) versus temperature.

The cross-talk factor for low gain is lower for cryogenic temperatures (left tail in figure 2.25). This can be explained by the fact, that at higher temperature more high energetic phonons are present. They increase the probability for an avalanche electron to emit a photon, which may lead to optical cross-talk. The raise at higher gain is not completely understood. The fact that it is stronger at low temperature can be explained by the shrinking of the diode and thus also of the space separating the individual micro-pixels. This increases the probability of both electric and optical cross-talk. We conclude that at low temperature the "MAPD-3N" should be used with not too high gain (in the range of $4.5 \cdot 10^4$ to $7 \cdot 10^4$).

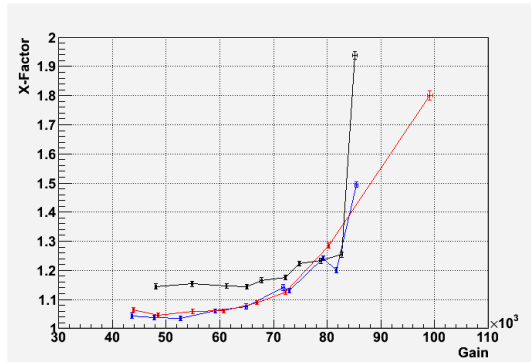


Figure 2.25: Cross-talk factor versus gain: blue- 77 K, red- 87 K, black- 298 K.

The noise-rate was measured in this low-gain-region at three temperatures (fig. 2.26). It was found, that at low temperature the noise-rate above 3p.e. is below 1 Hz, while it is above 1 kHz at room-temperature. The lower noise-rate at low temperatures is explained by the fact that less high energetic phonons are present. This lowers the probability of a thermal electron with enough energy to reach the conductive band and thus triggering an avalanche.

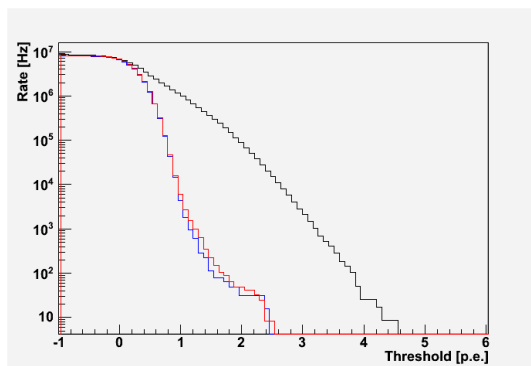


Figure 2.26: Noise-rate versus threshold at a gain of approximately $5.5 \cdot 10^4$: blue- 77 K, red- 87 K, black- 298 K.

Chapter 3

Cryogenic TPC readout system with a G-MAPD

To clarify open questions in today's neutrino-physics and in the search for Dark Matter many experiments rely on TPCs. Despite the wide range of physics to be covered with these experiments, they make use of the same technique. The LHEP Bern is involved in three projects using TPCs (the Ar-Tube experiments, the EXO experiment and the T2K near detector). Until now many different readout-systems have been developed and are used in these experiments. Depending on the medium used to fill the TPC and its aggregate state (gaseous, liquid or double-phase) different readout systems are possible today. Some of these readout systems provide an amplification already in the TPC medium while others collect the charge of the ionized track without amplification. Table 3.1 gives an overview of the most popular TPC readout-systems.

Readout system	Amplification	TPC medium
Wire plate	no	liquid
Wire plate	possible	gas
MicroMegas	yes	gas
(TH)GEM	yes	gas

Table 3.1: Different readout systems, with and without gain in the TPC medium.

To decrease the threshold of a TPC readout system its early state amplification is important. However, as can be seen in table 3.1, no readout system with amplification directly in the liquid TPC medium is presently known. Liquids (such as liquid Argon, Argon-Nitrogen mixture and Xenon) are however important due to their higher density and thus larger probability of particles interacting with them. To bypass the problem of amplification in liquid some TPCs use a double-phase technique. With this technique the ionizing particle leaves a charged track in the liquid-phase. This

charge is then extracted from the liquid into the gas-phase and read out with MicroMegas [12], GEMs [13] or THGEMs [14]. To reliably operate a double-phase TPC the liquid-level needs to be controlled very precisely and the surface at the phase-junction needs to be very flat. For large TPCs (as discussed in the LAGUNA-project) the flatness of the surface could be a critical point. Therefore the demand for a TPC readout system with amplification directly in the liquid-phase is obvious.

The novel approach of a TPC readout system, discussed here, the hybrid-field-induced-emission amplifier (HFIE), provides amplification in gas and liquid. In the framework of this thesis the HFIE, based on the G-MAPD (MAPD-3N), was partially explored in Argon gas. The effort of exploring and characterizing the HFIE in liquid Argon is going on at the LHEP Bern but is not covered by this thesis.

In this chapter first the before mentioned readout systems are explained in more details with the emphasis put on the HFIE. Later the experimental set-up, measuring-procedure and the so far obtained results, of a HFIE working in Argon gas, are presented. An outlook on the HFIE as a TPC readout-system is given in the end of this chapter.

3.1 The TPC and its readout systems

The Time Projection Chamber The Time Projection Chamber (TPC) is a particle tracking detector which allows three dimensional tracking of ionizing particles. If such a particle passes the active volume of the TPC it ionizes the atoms of the medium close to its path and leaves a track behind. The electrons and ions of this track are separated, due to the electric field (drift-field) between the cathode and the sensor-plane (anode) of the TPC (fig. 3.1).

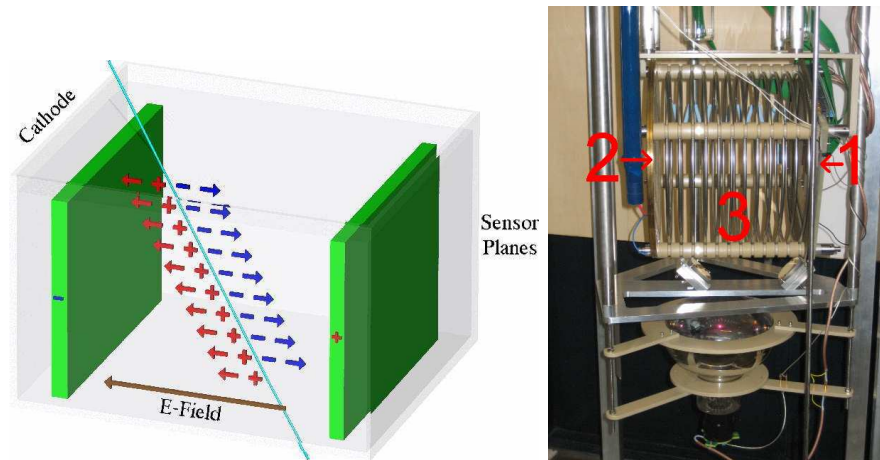


Figure 3.1: Schematic sketch of a TPC (left), indicating the free charge-carriers drifting in the electric field towards the the sensor-planes (electrons) and the cathode (ions) [15]. Photograph of the TPC used in the medium Ar-Tube experiment at LHEP Bern (right): 1- sensor-plane, 2- cathode, 3- field shaper rings.

The electrons reaching the sensor-plane are constantly read out by a readout system. This provides a two dimensional picture of the charge distribution at each moment. The third dimension is given by the time an electron needs to drift from the track to the sensor-plane. The third dimension is therefore continuously projected onto the sensor-plane (thus its name). Because the electrons have a larger mobility only they are read out and used for tracking.

As filling medium in TPCs mostly noble gases (gaseous or liquefied) are used. They hardly undergo chemical reactions and thus do not cause ageing. They are not flammable, not toxic and except for radon not radioactive. Free electrons have a long life time in noble gases because they are not electronegative. Noble gases are natural components of the earth atmosphere (tab. 3.2). Argon is the preferred choice in most cases because it's availability is high and thus its cost moderate.

Name	Chemical symbol	Mole fraction [%]
Nitrogen	N_2	78.09
Oxygen	O_2	20.95
<i>Argon</i>	<i>Ar</i>	0.93
Carbon dioxide	CO_2	0.03
<i>Neon</i>	<i>Ne</i>	$1.8 \cdot 10^{-3}$
<i>Helium</i>	<i>He</i>	$5.24 \cdot 10^{-4}$
<i>Krypton</i>	<i>Kr</i>	$1.0 \cdot 10^{-4}$
Hydrogen	H_2	$5.0 \cdot 10^{-5}$
<i>Xenon</i>	<i>Xe</i>	$8.0 \cdot 10^{-6}$
Ozone	O_3	$1.0 \cdot 10^{-6}$
<i>Radon</i>	<i>Rn</i>	$6.0 \cdot 10^{-18}$

Table 3.2: Chemical composition of dry air: italic- noble gases [16].

At the LHEP Bern three TPCs filled with liquid or gaseous Argon are presently operated. A forth one, the so-called "Big Ar-Tube", is under construction. It should give information about long drift-length (≈ 5 m) of the electrons in liquid Argon, witch is an important issue for a future large underground detector (discussed in the LAGUNA project).

At the Tokai to Kamiokande (T2K) experiment a near detector is installed with the purpose to measure the neutrino flux prior to its oscillation and to measure the poorly known neutrino interaction properties around 1GeV [17]. A central component of ND280 are three TPCs with MicroMegas readout systems. The medium in the ND280 is an Argon gas mixture (95% Ar, 3% CF_4 and 2% iC_4H_{10}).

The EXO experiment uses Xenon, enriched up to 80% with the isotope ^{136}Xe , witch is predicted to undergo double beta decay [18].

Wire-plane readout The wire-plane readout system consists of two wire planes. The wires of the two planes are oriented orthogonal to each other, allowing a spacial resolution in x- and y-direction. If the electrons pass the first plane (the so-called induction-plane) they induce a current in the wires closest to them. A few millimetres later the electrons are collected by the second wire-plane (the so-called collection-plane).

To prevent collection of the electrons already in the induction-plane it is set to the potential corresponding to the drift-field at its location. Figure 3.2 shows the wire-plane readout system of the medium Ar-Tube experiment at the LHEP Bern (using liquid Argon as medium for the TPC). The wire-plane readout system provides no internal gain but works reliably in gases and liquids.

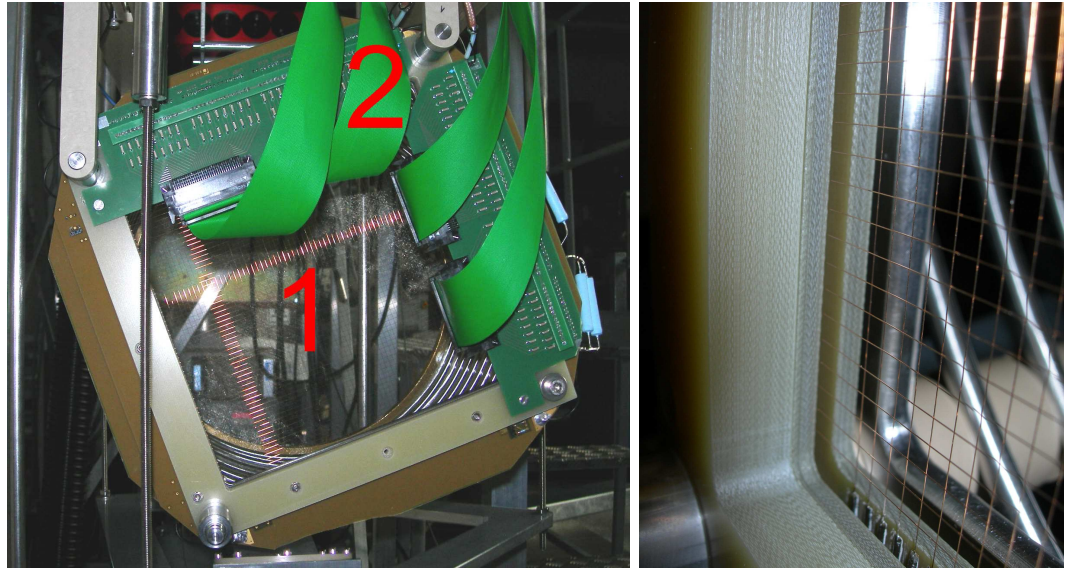


Figure 3.2: Photograph of the wire-plane readout system (left): 1- wires, 2- electric cables for signal read out. A close view to the wire-planes: vertical wires- induction-plane, horizontal wires- collection-plane.

MicroMegas readout The MicroMegas (MicroMESH Gaseous Structure) readout system consists of an anode-plane and a thin micromesh. Over the small gap (few $100 \mu\text{m}$) between them a high electric field is applied. The electrons of the primary track reaching the micromesh undergo acceleration in this field. If the field is high enough these electrons gain sufficient energy to ionize atoms of the gaseous TPC medium (the MicroMegas technique is intended only for use in gas). Thus in the gap an avalanche occurs evolving towards the anode-plane.

If the field is too high also the ions generated in this gap start to ionize atoms. This leads to a self-sustaining avalanche evolving in both directions, and break-down occurs. In a properly tuned avalanche the electrons are amplified and finally collected at the anode-plane. The anode-plane can be segmented into strips or pads allowing

a two dimensional read-out of the charge.

Figure 3.3 shows the MicroMegas readout-system used in the EXO experiment at LHEP Bern. As TPC medium Xenon or P10 (90% Argon, 10% Methane) gas are used. In some MicroMegas readout-systems also the micromesh is segmented. Thus the ions collected at the micromesh give additional information about the position of the particles track.

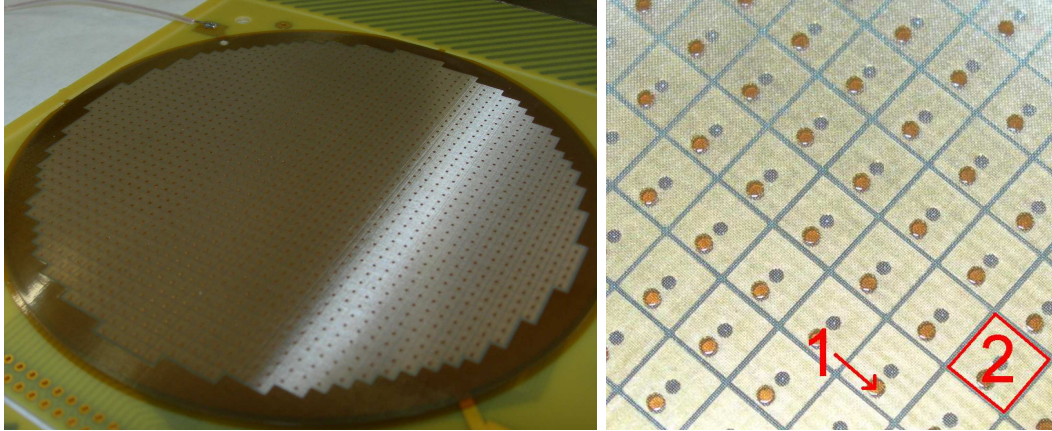


Figure 3.3: Photograph of the MicroMegas readout-system used in the EXO experiment at LHEP Bern (left) and a close look at the pads of the anode-plane with the micromesh installed above it: 1- a pillar to fix the micromesh $250 \mu\text{m}$ above the anode-plane, 2- a single pad ($3 \text{ mm} \times 3 \text{ mm}$).

GEM and THGEM readout The gas-electron-multiplier (GEM) is a gas ionization detector. The GEM works similar to the MicroMegas but has a different structure. It is build out of a thin ($50\text{-}70 \mu\text{m}$) Kapton sheet covered on both sides with a copper layer. Through this structure many small holes are etched (fig 3.4).

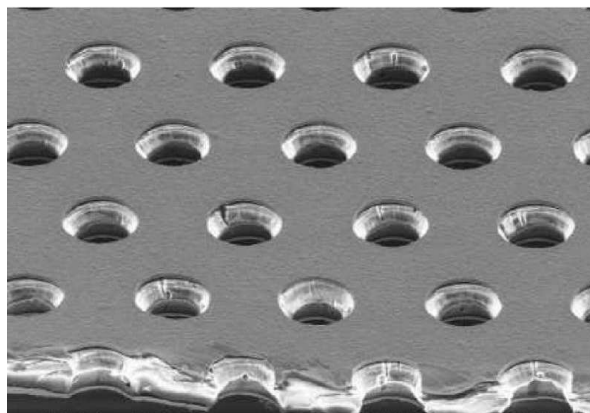


Figure 3.4: Electron microscope view of a GEM (hole diameter: $70 \mu\text{m}$)[13].

If a high voltage (few 100 V) is applied over the GEM, an electric field is generated in these holes. An electron of the primary track reaching the GEM undergoes multiplication in this field by ionizing atoms of the TPC medium (similar as in the MicroMegas readout-system). The electrons have to be extracted from the GEM with an additional electric field (extraction field) and read out at the segmented anode-plane. The gain achieved with a single GEM is in the range of 100 to 1000. To increase the gain often two or three GEMs are put in series (fig. 3.5).

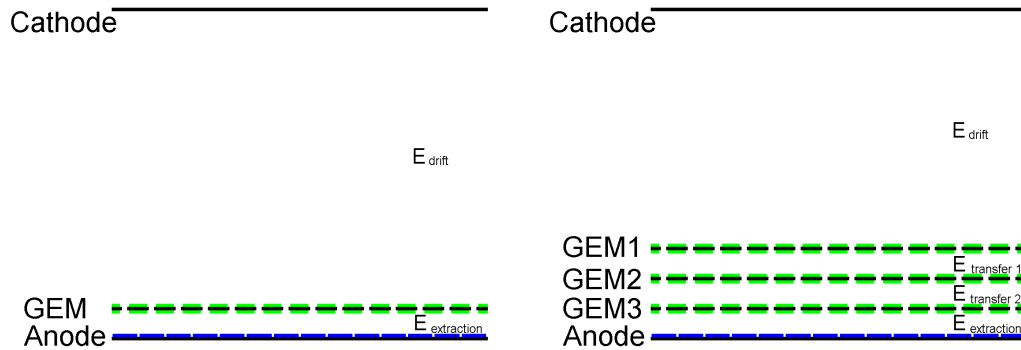


Figure 3.5: Sketch of a single (left) and triple GEM.

The thick-GEM (THGEM) is almost identical to the GEM but with 5 to 20 fold expanded dimensions (fig. 3.6). Because of their larger hole diameter a single THGEM provides a gain of up to 10^5 (with two THGEM's in series a gain of up to 10^7 can be achieved) [14].

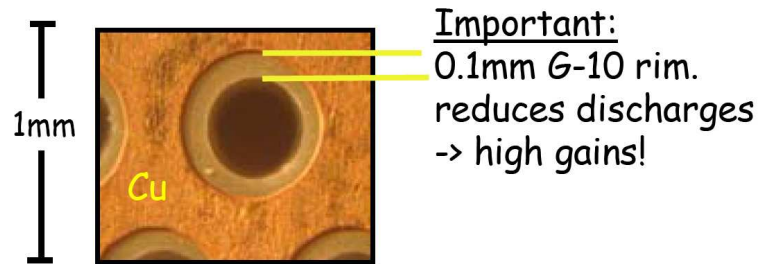


Figure 3.6: Close view on a THGEM[14].

The HFIE The hybrid-field-induced-emission amplifier (HFIE) is a novel type of TPC readout system. In contrast to the previously mentioned readout systems the HFIE doesn't collect charge directly, but via conversion to light. The electrons drift in a TPC (drift-section) towards a high electric field. In this field they undergo acceleration and stimulate atoms of the TPC medium to emit secondary scintillation light. This scintillation light is then collected with a photodiode (e.g. a G-MAPD). With this process electron-to-photon amplification takes place directly in the medium

of the TPC. The signal of the photodiode can then be read out and if needed amplified a second time. In figure 3.7 a sketch of a single HFIE channel is shown. The idea is to build a grid out of such devices and thus to have a 2D spacial resolution in the sensor-plane.

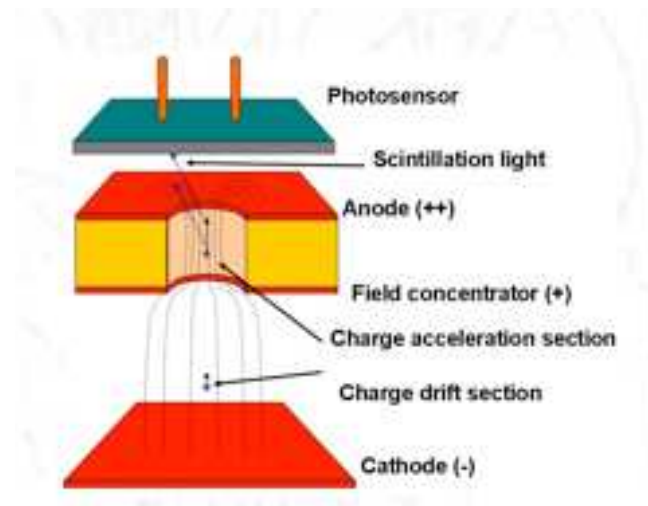


Figure 3.7: Sketch of the HFIE.

Depending on the particle ionization strength more or less atoms per unit length are ionized and thus collected by a single HFIE channel. After amplification a light signal with an intensity varying over a large range is present. The photodiode used to detect this light signal needs thus to have a large dynamic range. The micro-well structured G-MAPD's are well suited for this application thanks to their large pixel-density and capability to work at cryogenic temperatures.

3.2 The HFIE prototype, a novel approach of TPC read-out

Experimental set-up The HFIE prototype build at the LHEP Bern is made out of PCB plates ($3.5 \text{ cm} \times 3.5 \text{ cm} \times 0.8 \text{ mm}$) covered on both sides with a thin ($\approx 40 \mu\text{m}$) metal layer (fig. 3.8). The PCB technology is well known and standardised procedures, to manufacture PCB-print-boards on costumers demands are used today. Thus this technology allows an individual design at low cost.

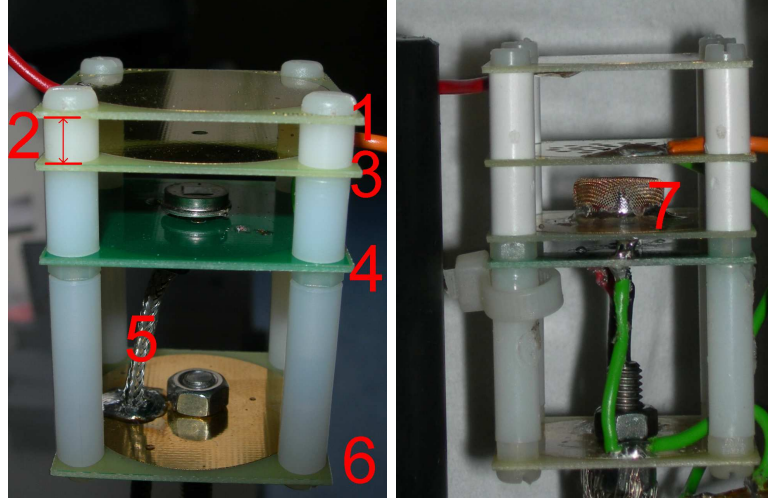


Figure 3.8: Photo of the basic HFIE set-up (left) and with later modification: 1- drift-plate, 2- drift-gap, 3- amplification-plate with a hole for the amplification-field, 4- the G-MAPD "MAPD-3N" soldered to the supply-plate, 5- shielded photodiode signal-line, 6- fixation of the HFIE to the top-flange of the dewar, 7- ground mesh to protect the G-MAPD from possible discharge in the hole.

The key part of the HFIE is the amplification-plate. To accelerate the electrons a very high voltage has to be applied over the two metal layers. The electric field in the hole must be close to the dielectric strength of the TPC medium. At the edges of the metal layers much higher local electric fields may appear than in the hole itself. This leads to corona effects at these edges and thus spontaneous discharge in the hole. Before the amplification-plate was build some finite-elements simulations were done with COMSOL multiphysics to study the electric-field in the region around the hole (fig. 3.9). The best results were achieved with a larger diameter for the holes through the metal layers and a smaller through the PCB. An insulation layer was put over the sharp edges of the metal layers to embed the parasitic high electric field existing there. This design was finally realised with different hole diameters. All the PCB plates used in the HFIE were made by the company TOMAPRINT GmbH in Baden-Dättwil, Switzerland. The manufacturing was however not very precise and the metal layer, drilled holes and printed insulation layer were displaced relative to each other. Thus most of the amplification-plates were of insufficient quality and could not be used. However a few of the amplification-plates without the insulation-layer could still be used.

Electric field, norm [MV/m]

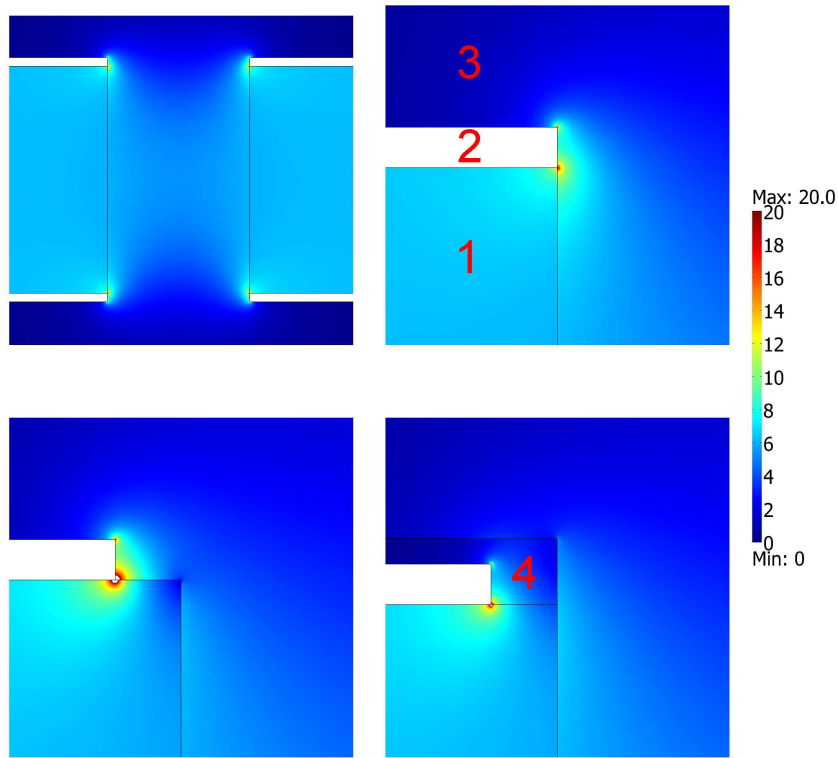


Figure 3.9: Finite element simulation of the electric field in three different hole types (inner hole diameter 1 mm). Basic structure (top-left) and magnifications of the edges in: the drilled through (top-right), different diameter for holes in the metal layer and in the PCB without (bottom-left) and with (bottom-right) insulation layer. 1- PCB plate, 2- metal layer, 3- medium, 4- insulation layer.

To test the HFIE a vacuum tight, thermal insulated volume filled with gaseous or liquid Argon was needed. For this purpose a dewar (the so-called μ -Ar-Tube) was designed and manufactured at the LHEP workshop (for more details on the μ -Ar-Tube see Appendix B). The μ -Ar-Tube consists of an insulation vacuum gap with super-isolation, an outer and an inner bath where the HFIE was mounted. To apply the electric fields in the hole (amplification-field: HV-) and the drift-region (drift-field: HV--), two high-voltage-supplies (ISEG HPn 300 106 and FUG HCN 140-35000) were used. Each voltage was protected with a resistor (1 G Ω to quench a possible discharge) connected over a high-voltage-feed-through to the HFIE. The HFIE itself is fixed with a rod to the top-flange (fig. 3.10). If the μ -Ar-Tube is closed the HFIE is located close to the bottom of the inner bath.

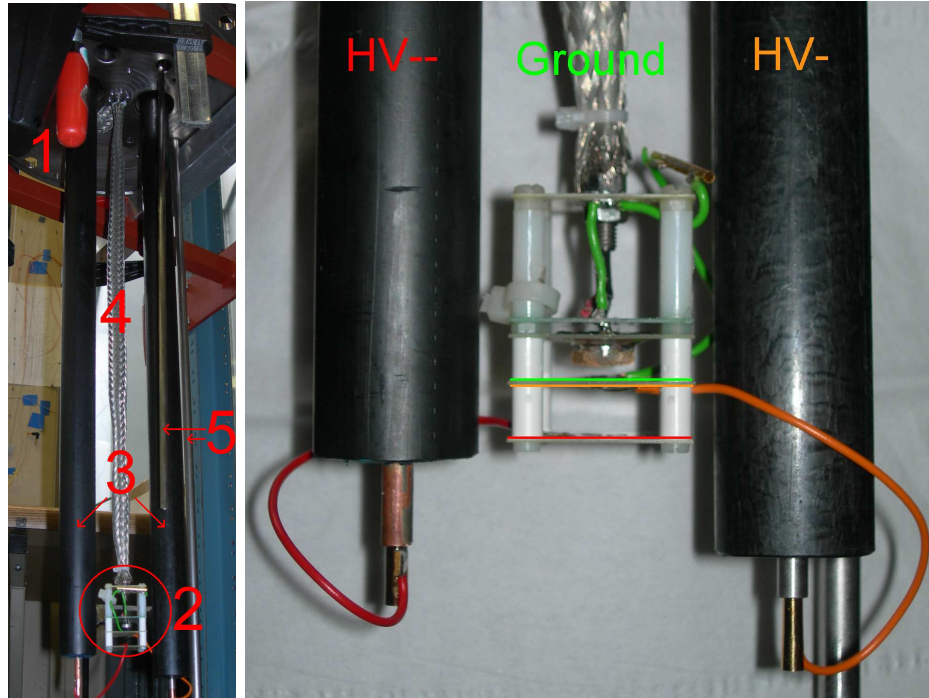


Figure 3.10: Worm's-eye view of the top-flange (left) and close view on the mounted HFIE: 1- top-flange, 2- HFIE, 3- high-voltage-feed-through, 4- shielded data-line of the G-MAPD fixed to the rod, 5- level-meters.

To control the gas or liquid a pressure-meter, an over pressure valve (security), a vacuum-probe, a filling line for the gas or liquid, a level-meter (used with liquid only), and a gas exhaust were installed for both baths. The top-flange provides additional feed-throughs for the data readout of the G-MAPD and the LED cable. Figure 3.11 shows a close view at the top-flange of the μ -Ar-Tube.

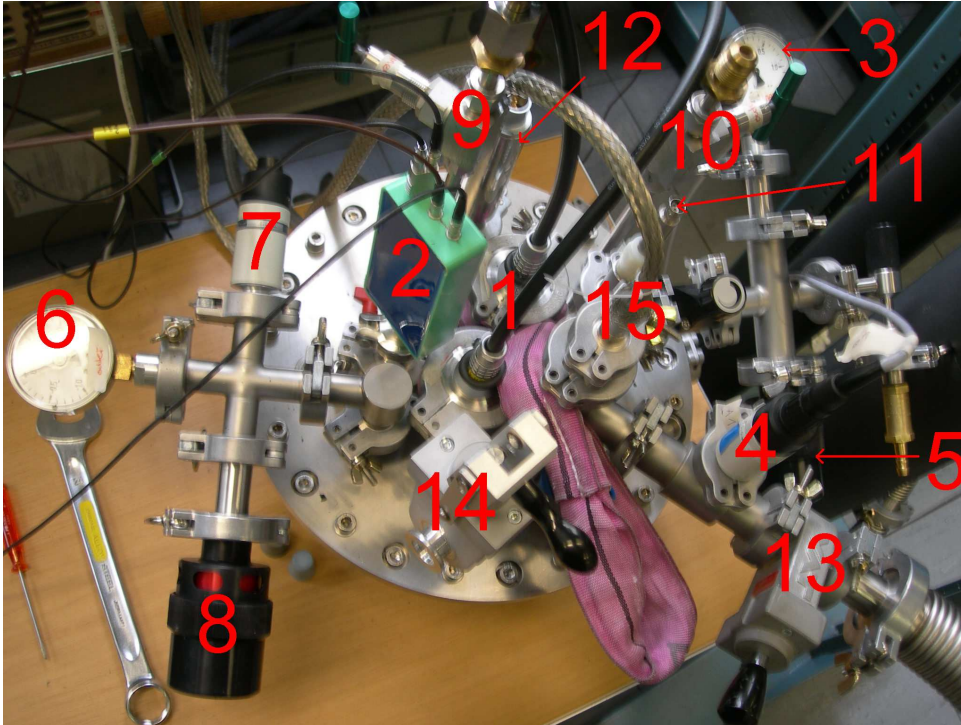


Figure 3.11: Close view at the top-flange of the μ -Ar-Tube: 1- high voltage connectors for the drift and amplification field, 2- box containing the pre-amplifier "AMP_0604" (Photonics SA), 3 to 5- manometer, vacuum-probe and overpressure valve of the inner bath, 6 to 8- manometer, vacuum-probe and overpressure valve of the outer bath, 9 and 11- filling line and level-meter for the inner bath, 10 and 12- filling line and level-meter for the outer bath, 13- gas exhaust and vacuum line of the inner bath, 14- gas exhaust of the outer bath, 15- connector for the LED, only used for G-MAPD testing.

To increase the purity of the Argon, the dewar was evacuated with a roots-pump and a pre-vacuum-pump before it was filled through a filter, for oxygen-trapping (*OXYSORBTM*), with gaseous or liquid Argon. Figure 3.12 shows an overview of the complete set-up.

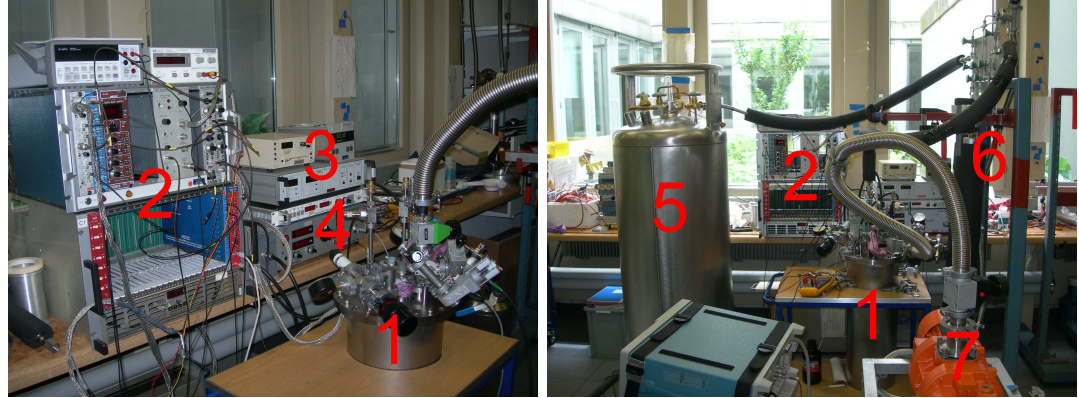


Figure 3.12: Photograph of the set-up used to test the HFIE: 1- μ -Ar-Tube, 2- electronics for data processing and readout, 3- display of the level-meters and vacuum-probe, 4- high-voltage-supplys and boxes with $1\text{G}\Omega$ quenching resistors, 5- ranger containing up to 200 litres of liquid Argon, 6- filter, 7- vacuum-pump.

The signal of the G-MAPD was amplified outside the dewar with of a pre-amplifier "AMP_0604" (Photonics SA). The signal processing was done identically to the noise-rate-spectrum measurements of the G-MAPD (described in section 2.2). The threshold at the discriminator was set to approximately three-photo-electrons at the G-MAPD.

Data taking The HFIE was tested in gaseous and liquid Argon but only in gas results were acquired so far. In liquid Argon break-down and corona effects occurred before a high amplification-field was reached. The HFIE used in this thesis is still in the development phase and not yet mature. All the measurements are presented in arbitrary units and should give the proof of the HFIE's working-principle in Argon gas. However no quantitative statements are made.

To test the HFIE in gas Argon a foil with an alpha-source (^{241}Am emitting alpha-particles of 5.5MeV) was soldered onto the drift-field-plate of the HFIE (fig. 3.13). The alpha-particles were emitted directly in the drift-gap and produced an ionized track. The electrons of this track drifted towards the hole in the amplification-plate and were then read out by the HFIE.

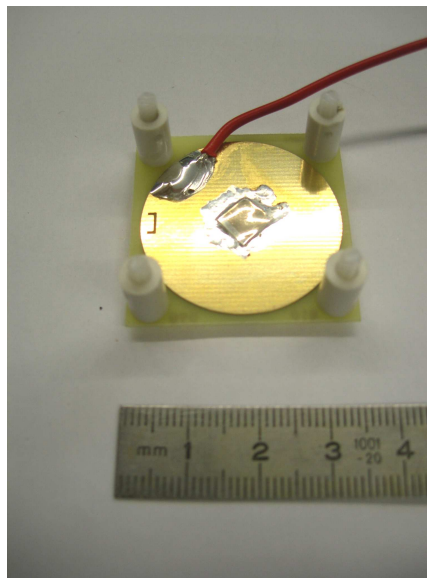


Figure 3.13: Photograph of the drift-plate with the alpha-source soldered on it.

At a pressure of 1 bar the alpha-particles reached the G-MAPD and caused a parasitic response (distance between the alpha-source and the G-MAPD: ≈ 1.5 cm). To stop the alpha-particles before they reach the G-MAPD the pressure in the dewar was increased to 4bar (the range of alpha-particles with 5.5MeV at 4bar in air, which is similar to Argon gas, is approximately 1 cm). This reduced the signal rate from approximately 10 Hz (1 bar) below 0.1 Hz (4 bar), with no fields applied. At this pressure two series of measurements were taken, one with the alpha-source and one without. Figure 3.14 shows the results of these measurements at different amplification-fields. Reversing the drift-field in the measurements with the alpha-source decreased the rate significantly (below 1 Hz).

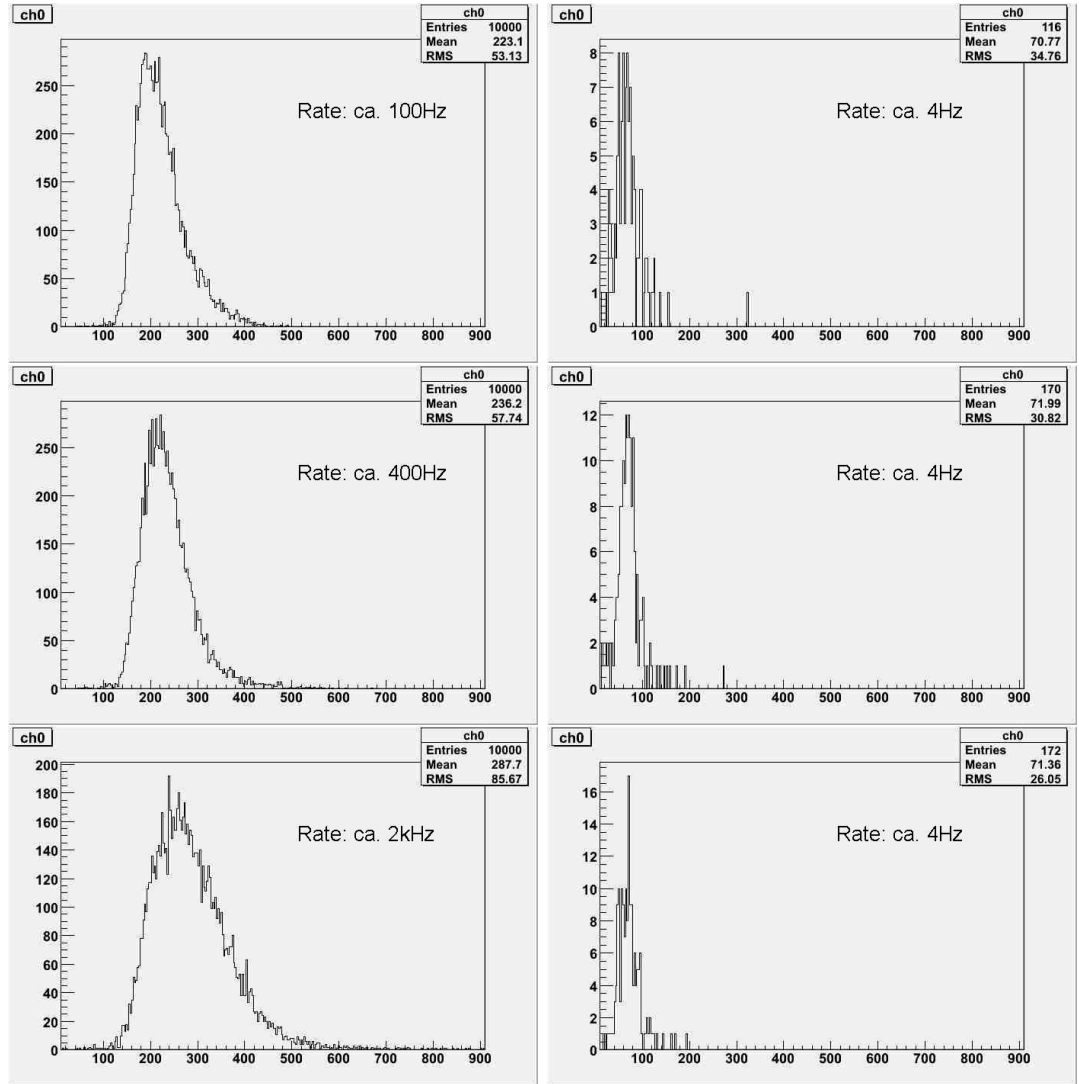


Figure 3.14: Data taken in 4 bar Argon gas with the alpha-source (left) and without (all plots in arbitrary units): top- HV(-) -2.5 kV and HV(-) -3.0 kV, middle- HV(-) -2.7 kV and HV(-) -3.2 kV, bottom- HV(-) -3.0 kV and HV(-) -3.5 kV.

The data taken does not allow any quantitative statements on the HFIE's working in Argon gas. However out of the measurements presented in figure 3.14 it is obvious that the alpha-source influences the measurements significantly. Thus the possibility that the signal is due to corona effects or spontaneous discharge in the hole of the HFIE can be excluded (otherwise it would also occur without the alpha-source). Due to the rate decreasing significantly with a pressure of 4bar, it can also be concluded that the signal observed is not due to alpha-particles hitting directly the G-MAPD. Furthermore the observed signal vanishes with reversed drift-field (leaving the amplification-field unchanged). This indicates that the observed signal is due to

electrons reaching the amplification-field. In further agreement with the expectation is the larger signal with larger amplification-field (the peak moves to the right with a higher amplification-field) but not the increasing rate.

Thus it can be concluded that the HFIE prototype realised at the LHEP Bern works in Argon gas. It is however not mature and more tests need to be done to gain a better understanding of this device. A probable reason for the early break-down in liquid Argon is the missing insulation-layer on the amplification-plate.

Chapter 4

Conclusions and outlook

In the framework of this master thesis a special silicon photon detector, the so-called Geiger-mode micro-pixel avalanche photo-diode (G-MAPD), was systematically characterized at ambient and cryogenic conditions. For this purpose an experimental set-up was realized by the candidate, including a valve to control automatically the level of the cryogenic liquids.

In this thesis it is shown for the first time that a micro-well structured G-MAPD (the "MAPD-3N" from Zecotek, Russia) can be operated at cryogenic temperatures with a resolution good enough to detect single-photons. In particular, it is found that the "MAPD-3N" works even better at cryogenic temperature than at ambient temperature, if operated with a internal gain below $7 \cdot 10^4$. Namely, the cross-talk and the noise-rate are smaller under cryogenic conditions.

Therefore, as a main achievement of this thesis, we conclude that with the "MAPD-3N" a solid-state photon-detector with single-photon resolution is available, which works well at cryogenic conditions. This is an important step towards replacing photomultiplier tubes with G-MAPDs and opens many new possibilities for low temperature applications.

Furthermore, a novel readout system for Time Projection Chambers (TPCs), the so-called hybrid-field-induced-emission amplifier (HFIE), was partially explored for operation in Argon gas. For this purpose, a HFIE prototype making use of the "MAPD-3N" and a double walled dewar, a small drift-chamber, a DAQ system and the related analysing software, was designed and realized by the candidate with contributions of the LHEP team.

The data taken with the HFIE prototype do not allow yet quantitative statements on the HFIE operated in Argon gas. However, as an achievement of this thesis, it can be concluded that the HFIE works well in Argon gas. The HFIE prototype is however not mature, and more tests need to be done to gain a better understanding of the device.

Recently (2009) P.K. Lightfoot et al. have for the first time observed and measured secondary scintillation generated within a HFIE immersed in liquid Argon [19]. The HFIE seems to be a promising TPC readout system with an early state amplification.

Low threshold TPC readout can be achieved by it, which is an important issue in the search of Dark Matter and in the measurement of neutrino interactions.

Appendix A

Construction of the automatic level regulating valve

To characterise the G-MAPD in a cryogenic environment a bath filled with liquid Nitrogen (LN) or liquid Argon (LAr) was build. Due to evaporation of the liquids and the small volume of the bath (less then 1 dl) its level decreased rapidly and refilling was necessary. The idea had come up to build a valve which regulates the level in the bath. With the help of this valve the level could be adjusted and kept stable (± 3 mm). In figure A.1 a layout of the the valve is shown.

It consists of three main parts: a massive block where the copper tube (filling line) from the tank was connected to, a bolt which opened and closed the valve and a floater made out of Styrofoam connected to the bolt to lift it if the liquid level is high enough. This design of the valve was not sensitive to a small overpressure in the filling line (e.g. barometric pressure). To make the valve tight in closed position a very high manufacturing precision (1/100 mm) for the bolt and its hole in the massive block was needed.

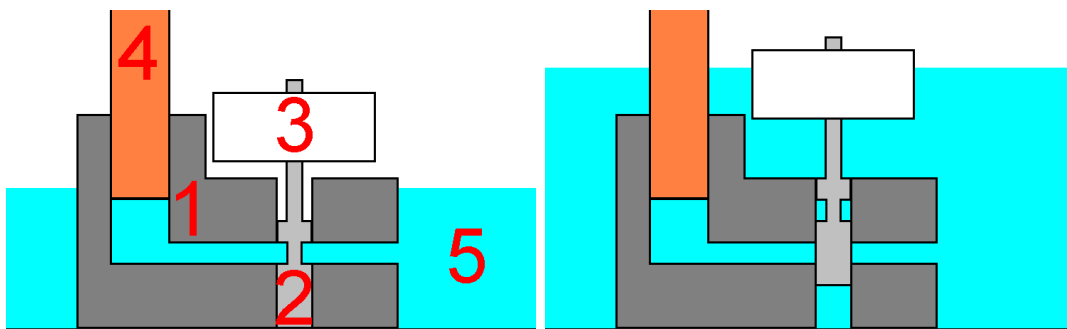


Figure A.1: Layout of the automatic level regulating valve in opened position (left) and closed position (right): 1- massive block, 2- bolt, 3- floater, 4- copper tube, 5- liquid noble gas.

The first such valve build (see figure A.2) had a clear problem. It was planned to be used with a copper tube of 4 mm inner diameter. But the maximum flux through this tube was not high enough to cool down the massive block and the bath in an useful time.

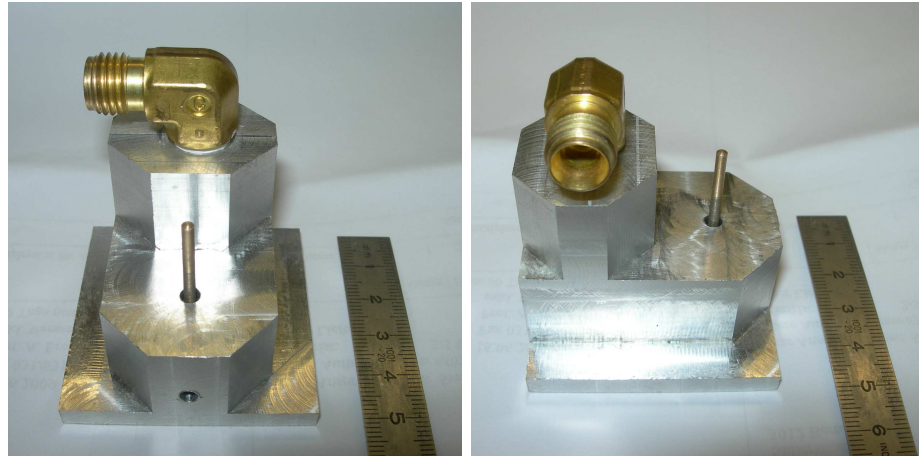


Figure A.2: Photo of the first valve prototype with the floater dismounted.

For the second attempt the design changed almost completely, only the bolt stayed identical (see figure A.3). An upper touch for the bolt was added to fix it properly to the massive block. It was designed to be used with a copper tube of 6 mm inner diameter. The tests showed that the flux through this tube is sufficient. But from time to time it happened that the bolt stuck in the massive block and the valve blocked in ether closed or open position. This was the result of using two different metals with different heat expansion coefficient for the massive block (aluminium) and the bolt (brass).

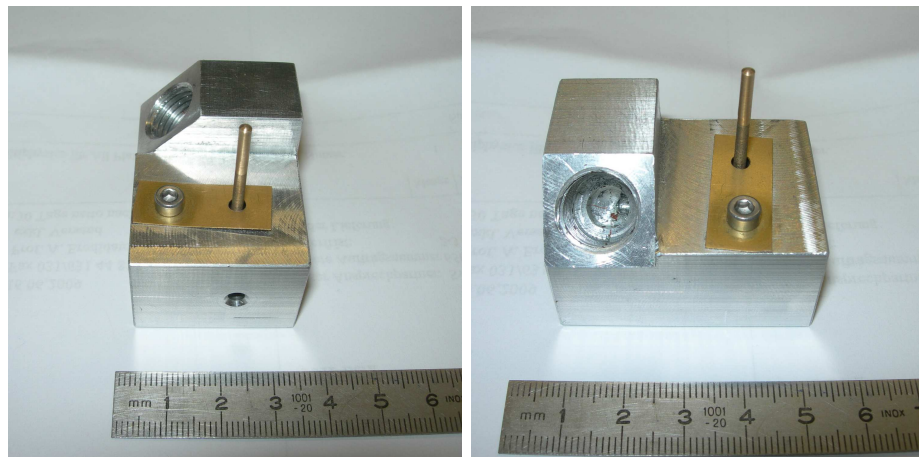


Figure A.3: Photo of the second valve prototype with the floater dismounted.

The final valve had almost the same design as the second one but was completely made out of brass which solved the problem of blocking the valve. The floater was fixed with two rubber pieces to the bolt. The level of the bath could be set by adjusting the position of the floater with respect to the bolt. Some additional weight was put on the floater to increase the gravitational force pulling down the bolt and closing the valve (see figures A.4 and A.5). As an improvement to the prior valve a guide for the Styrofoam floater was added to prevent it from rotating and thus possibly blocking.

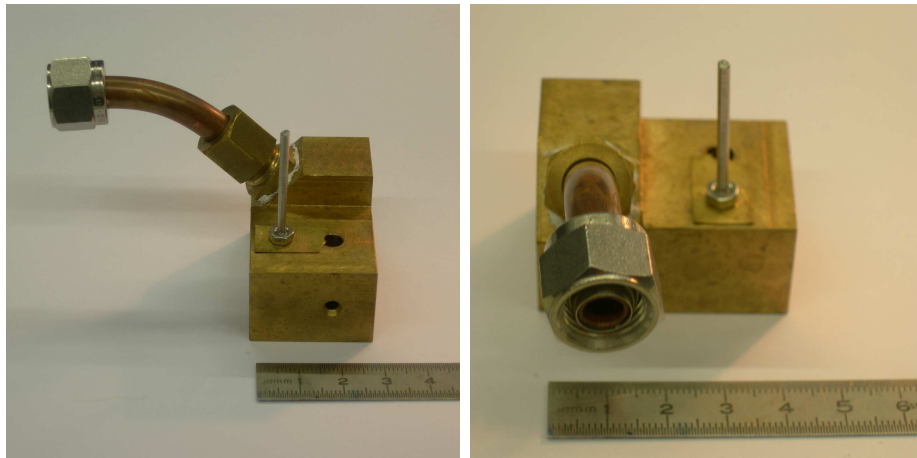


Figure A.4: Photo of the final valve with the bolt dismounted.

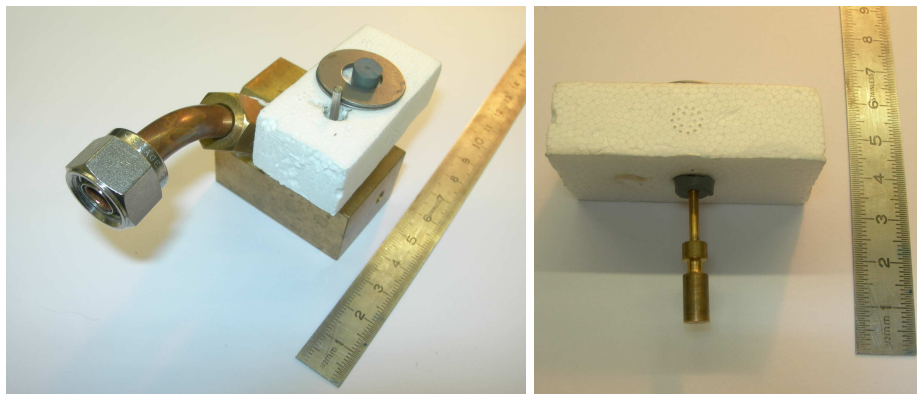


Figure A.5: Photo of the complete final valve with washers as additional weight (left) and the bolt with Styrofoam floater (right).

Appendix B

Construction of the μ -Ar-Tube

To test the HFIE in gas and in cryogenic liquids a double-bath dewar was designed and constructed at LHEP Bern. This dewar provides a very good thermal insulation to minimize the evaporation of the cryogenic liquids. The μ -Ar-Tube consists of a double-walled vessel (a so-called dewar) and a cartridge (fig. B.2). A top-flange to close the dewar was also build, it provides several feed-throughs for the experimental needs (fig. B.1). The μ -Ar-Tube was designed to be used with a cartridge. Optionally it can however be used without this cartridge and still closes vacuum-tight (e.g. if a larger experimental space would be needed in a later experiment).

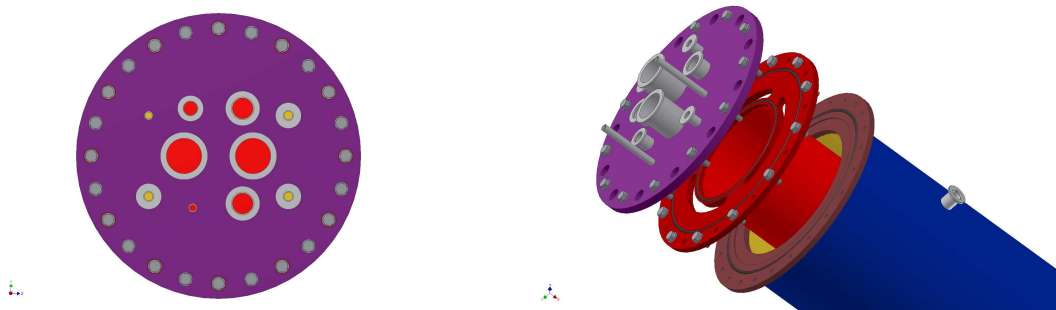


Figure B.1: View on the top-flange with feedthroughs to the inner (red) and outer (yellow) bath (left) and an exploded view drawing of the top part(right).

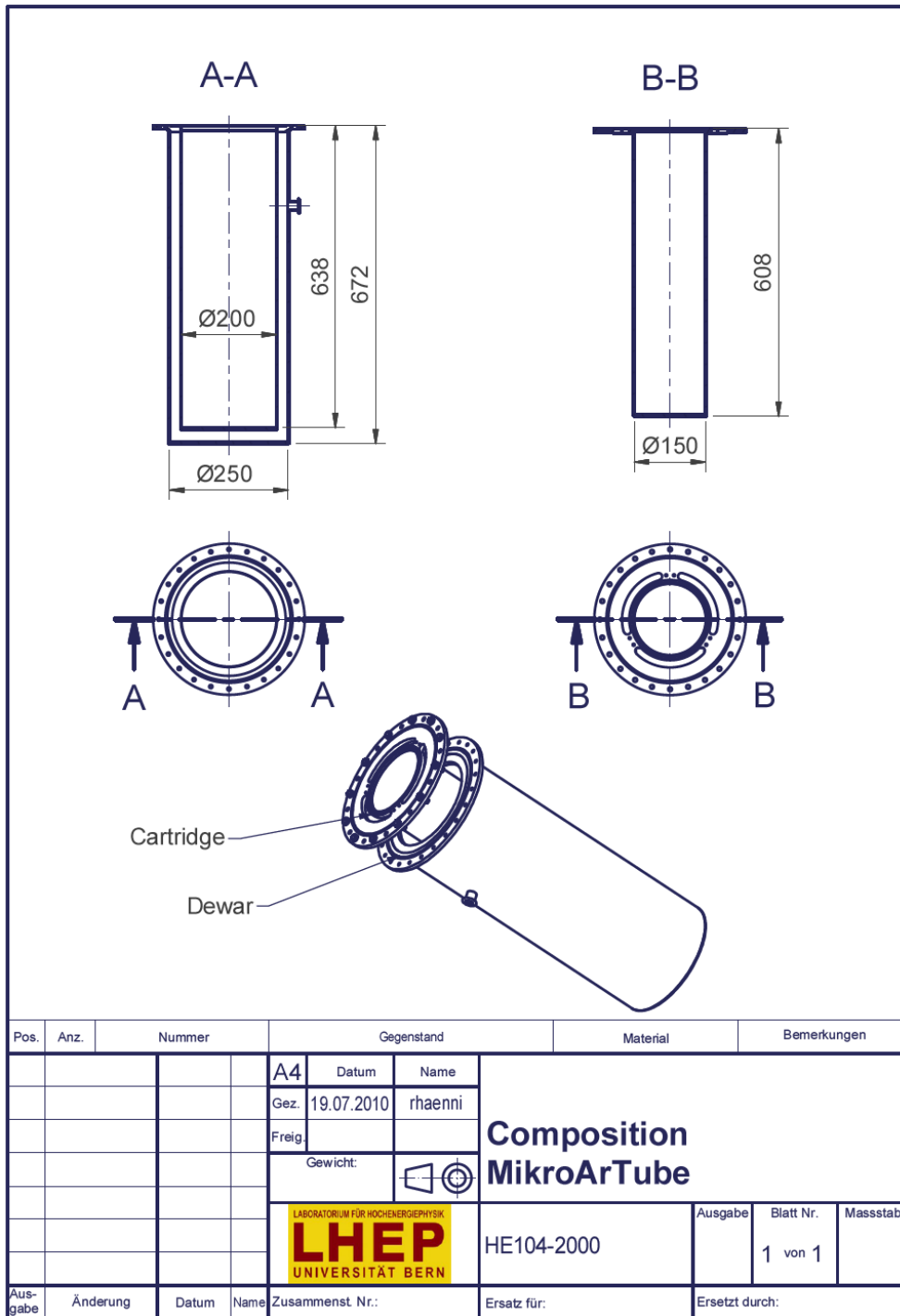


Figure B.2: Technical drawing of the dewar and the cartridge (dimensions in mm).

Before the μ -Ar-Tube was build at the workshop of LHEP Bern several things had to be clarified:

- Which material should be used to construct the μ -Ar-Tube
- How thick should be the walls of the dewar and cartridge
- Is super-insulation needed or not

To answer these questions the influence of these three points on the heat exchange with the environment were estimated. As a reference work a script of Prof.Dr.S.Janos [20] was used. Also his expertise on low temperature technique was very helpful.

Heat-exchange with the environment Heat exchange with the environment occurs in three forms:

- Heat-conduction
- Heat-radiation
- Convection

After evacuating the gap between the inner and outer walls of the dewar, heat-conduction between them is prevented. Nevertheless the inner tube is connected to the top of the dewar, which is in direct thermal contact with the surrounding warm air. Heat-exchange through the heat conducting walls can not be completely prevented. The heat-exchange through heat-conduction can be calculated by the relation

$$\dot{Q} = (A/L) \cdot (I(T_h) - I(T_l)). \quad (\text{B.1})$$

Where \dot{Q} denotes the heat flow, A the cross section area, L the length of conductor. I the thermal-conductivity-integral, T_h the temperature at the warm end and T_l at the cold one. The thermal-conductivity-integral (tab. B.1) is used because the thermal-conductance can not any more be simplified by a constant if used in a range above 200K. Considering the last row in table B.1 it was clear that only stainless steal and glass can be used to build the μ -Ar-Tube (glass drops out due to mechanical stability and machinability). Using copper instead of stainless-steel (aluminium) [glass] would lead to a 34 (16) [0.07] times larger heat-flow accordingly. This would result in a very rapid evaporation and constant boiling of the cryogenic liquids.

Considering the factor A/L in the relation B.1 the walls should be as thin as possible. These walls however need to withstand a pressure of up to 4bar. Thus as a compromise between heat-flow and mechanical stability stainless steel tubes with 2 mm thick walls were used to build the μ -Ar-Tube. The heat flow due to heat-conduction and the equivalent evaporation of liquid Argon (latent heat: 224[kJ/l]) and liquid Nitrogen (latent heat: 160[kJ/l]) was calculated (filled 10 cm below the top).

Temp. [K]	Cu	Al	Brass	Stainless steel	Glass
77	58600	15800	1620	317	11.2
90	65400	19000	2200	436	24.0
300	152000	61300	17200	3060	199
I(300)-I(77)	93400	45500	15580	2743	181.5

Table B.1: Table of thermal-conductivity-integrals in watt/meter [20].

$$\dot{Q} = 61 \text{ watt} \Rightarrow 0.98 \text{ litre Argon per hour} \hat{=} 1.37 \text{ litre Nitrogen per hour} \quad (\text{B.2})$$

The heat-flow due to radiation is described by the Stefan-Boltzmann law:

$$\dot{Q} = \sigma \varepsilon \cdot T^4 \quad (\text{B.3})$$

Where \dot{Q} denotes the heat flow, σ the Stefan-Boltzmann-constant ($5.67 \cdot 10^{-8} \text{ W m}^{-2} \text{ K}^{-4}$) and ε the emissivity of the radiating surface (tab. B.2). Out of the Stefan-Boltzmann law a formula for the heat-flow, due to radiation between two equal sized surface, was derived

$$\dot{Q} = A \cdot \sigma \cdot \frac{\varepsilon^2}{2 \cdot \varepsilon - \varepsilon^2} \cdot (T_h^4 - T_l^4). \quad (\text{B.4})$$

With this formula the heat-flow due to heat-radiation was calculated (using the emissivity of stainless steel):

$$\dot{Q} = 11 \text{ watt} \Rightarrow 0.18 \text{ litre Argon per hour} \hat{=} 0.25 \text{ litre Nitrogen per hour} \quad (\text{B.5})$$

It is remarkable that for glass the heat-flow due to radiation (165 watt) is a factor 38 larger than the one due to conduction (4.3 watt).

To calculate the heat-flow due to radiation with super-insulation ($\approx 6 \mu\text{m}$ thin crinkled aluminized Mylar foil) the formula B.6 was used.

$$\dot{Q} = (A/N) \cdot (6.5 \cdot 10^{-14} \cdot (T_h^4 - T_l^4) + 2.7 \cdot 10^{-11} \cdot D^{1.5} \cdot (T_h - T_l)) \quad (\text{B.6})$$

Where A denotes the area of one of the radiating surfaces, N the number of Mylar layers and D the layer density in sheets per inch. With this formula the heat-flow due to heat-radiation with 10 layers super-insulation was calculated (D = 25 sheets / inch):

$$\dot{Q} = 0.6 \text{ watt} \Rightarrow 9.6 \text{ millilitre Argon per hour} \hat{=} 13.5 \text{ millilitre Nitrogen per hour} \quad (\text{B.7})$$

Material	Condition	emissivity
Cu	polished, clean	0.02
Cu	highly oxidized	0.6
Al	wire brushed, steel wool	0.06
Al	polished, heavy anodized	0.32
Brass	polished, clean	0.03
Brass	highly oxidized	0.6
Stainless steel	polished	0.06
Glass		0.9

Table B.2: Emissivity of different materials and conditions [20].

Considering these calculations for the heat-flow due to conduction and radiation we decided:

- To build the μ -Ar-Tube out of stainless steel
- As a compromise the walls should be 2 mm thick
- To use 10 layers of super-insulation

Heat-flow due to convection was neglected because it is not affected by any of these points. Figure B.3 shows three photos of the finished μ -Ar-Tube.



Figure B.3: The cartridge of the μ -Ar-Tube (left), mounted in the dewar (middle) and with the fully equipped top-flange mounted.

List of Figures

1.1	Schematic view of a photo-multiplier-tube.	5
1.2	Simple voltage-divider soldered directly on to the electrical connectors of a PMT (the Hamamatsu R7725 MOD used in the small LAr TPC experiment at LHEP Bern).	5
1.3	Three PMTs of different size next to a 20 cm long ruler: the Hamamatsu R5912-02MOD used in the medium LAr TPC experiment at LHEP Bern (left), the Philips 53AVP which is similar in size to the Hamamatsu R7725 MOD (middle), the Hamamatsu R1450 used for some test runs in the small LAr TPC (right).	6
1.4	Schematic of a p-n-junction (modification of [3]).	7
1.5	Current-voltage-diagram of a p-n-junction [5].	8
1.6	The absorption-length of photons in silicon depending on their wavelength [6].	9
1.7	Structure of a PIN-diode [1].	10
1.8	Structures, electric field and electron/hole multiplication for (left) bevelled-edge, (middle) reach-through and (right) shallow junction APDs (modified from [9]).	11
1.9	Schematic views of the surface-resistor (top) and the micro-well structure of G-MAPD's: 1- common metal electrode, 2- buffer layer of silicon oxide, 3- p-n-junctions/micro-pixels, 4- individual surface resistors, 5- epitaxial silicon layer of p-type conductivity, 6- a high-doped silicon layer of p-type conductivity, 7- a region with micro-wells, 8- local avalanche regions, 9- individual micro-wells. (Modified from [1] which is a reprint from [10]).	13
1.10	The pulse-height-spectrum of low intensity light pulse recorded with a G-MAPD Hamamatsu 1-53-1A-1 (left, modified [1]) and a PMT [11]. All axes in arbitrary units.	13
1.11	Plot of the function describing the characteristic pulse-height-spectrum of a G-MAPD. The gain is indicated in red.	14
2.1	The "AMP_0604" (Photonics SA) with the "MAPD-3N" (Zecotek) mounted.	15

2.2	Photo of the experimental set-up: 1- box with G-MAPD inside, 2- insulated tank for the cryogenic liquids, 3- electronics for light pulse generation and signal readout, 4- PC for data acquisition (DAQ), 5- oscilloscope used as a monitoring device.	16
2.3	Photo of the open box (left) and the cover (right): 1- G-MAPD with shielding , 2- pre-amplifier wrapped in a shielding in thermal contact with a heat-exchanger, 3- light conductor , 4- automatic level control valve inside the bath for the cryogenic liquids.	16
2.4	Picture of the oscilloscope screen: blue- signal of the G-MAPD after full amplification, yellow- gate for the integrator.	17
2.5	Schematic of the data flow used for pulse-height spectrum measurements.	18
2.6	Photo of the NIM-rack (left) and CAMAC-rack: 1- amplifier , 2- discriminator , 3- HV-supply for bias-voltage , 4- rate-meter , 5- LED-generator , 6- dual-timer , 7- ADC integrator card , 8- link card. . . .	18
2.7	Schematic of the data flow used for noise-rate spectrum measurements.	19
2.8	Diagram of the circuit used to inject the charge.	19
2.9	Schematic of the data flow used for calibration.	19
2.10	Examples of a pulse-height (left) and noise-rate spectrum (right) before post-processing.	20
2.11	Response of the circuit to the injected charge: -black at 0 mV amplitude, blue- at 15 mV, red- at 30 mV.	20
2.12	Mean values of the response of the circuit to the injected charges (the errors of the mean values are very small can not be seen here). . . .	21
2.13	Calibration curve, mean values of the circuits response versus the injected charges (in units of e, the electron charge).	21
2.14	Pulse-height spectrum after scaling the x-axis.	22
2.15	Pulse-height-spectrum with the function $f(x)$ fitted to the measured curve.	22
2.16	Pulse-height-spectrum measured at 87 K with different bias voltages: -78.397 V, -78.602 V, -78.798 V, -79.000 V (left to right, top to bottom).	23
2.17	Gain versus bias-voltage for three temperatures: blue- 77 K, red- 87 K, black- 298 K.	23
2.18	Breakdown voltage (left) and slope of the gain (right) versus temperature.	24
2.19	A Gaussian fitted to the pedestal peak of a pulse-height spectrum (with p_0 the number of pedestal entries and the mean value of the total spectrum).	25
2.20	Cross-talk factor versus gain: blue- 77 K, red- 87 K, black- 298 K. On the right side for better clarity normalized to one.	25
2.21	Noise-rate spectrum (left) and integrated (right). Measured at 298 K with -89.5 V bias voltage applied.	26
2.22	Noise-rate versus threshold at a gain of approximately $5.5 \cdot 10^4$: blue- 77 K, red- 87 K, black- 298 K.	26
2.23	Gain versus bias voltage for three temperatures: blue- 77 K, red- 87 K, black- 298 K.	27

2.24	Breakdown voltage (left) and slope of the gain (right) versus temperature.	27
2.25	Cross-talk factor versus gain: blue- 77 K, red- 87 K, black- 298 K.	28
2.26	Noise-rate versus threshold at a gain of approximately $5.5 \cdot 10^4$: blue- 77 K, red- 87 K, black- 298 K.	28
3.1	Schematic sketch of a TPC (left), indicating the free charge-carriers drifting in the electric field towards the the sensor-planes (electrons) and the cathode (ions) [15]. Photograph of the TPC used in the medium Ar-Tube experiment at LHEP Bern (right): 1- sensor-plane, 2- cathode, 3- field shaper rings.	30
3.2	Photograph of the wire-plane readout system (left): 1- wires, 2- electric cables for signal read out. A close view to the wire-planes: vertical wires- induction-plane, horizontal wires- collection-plane.	32
3.3	Photograph of the MicroMegas readout-system used in the EXO experiment at LHEP Bern (left) and a close look at the pads of the anode-plane with the micromesh installed above it: 1- a pillar to fix the micromesh 250 μm above the anode-plane, 2- a single pad (3 mm \times 3 mm).	33
3.4	Electron microscope view of a GEM (hole diameter: 70 μm)[13].	33
3.5	Sketch of a single (left) and triple GEM.	34
3.6	Close view on a THGEM[14].	34
3.7	Sketch of the HFIE.	35
3.8	Photo of the basic HFIE set-up (left) and with later modification: 1- drift-plate, 2- drift-gap, 3- amplification-plate with a hole for the amplification-field, 4- the G-MAPD "MAPD-3N" soldered to the supply-plate, 5- shielded photodiode signal-line, 6- fixation of the HFIE to the top-flange of the dewar, 7- ground mesh to protect the G-MAPD from possible discharge in the hole.	36
3.9	Finite element simulation of the electric field in three different hole types (inner hole diameter 1 mm). Basic structure (top-left) and magnifications of the edges in: the drilled through (top-right), different diameter for holes in the metal layer and in the PCB without (bottom-left) and with (bottom-right) insulation layer. 1- PCB plate, 2- metal layer, 3- medium, 4- insulation layer.	37
3.10	Worm's-eye view of the top-flange (left) and close view on the mounted HFIE: 1- top-flange, 2- HFIE, 3- high-voltage-feed-through, 4- shielded data-line of the G-MAPD fixed to the rod, 5- level-meters.	38

3.11	Close view at the top-flange of the μ -Ar-Tube: 1- high voltage connectors for the drift and amplification field, 2- box containing the pre-amplifier "AMP_0604" (Photonics SA), 3 to 5- manometer, vacuum-probe and overpressure valve of the inner bath, 6 to 8- manometer, vacuum-probe and overpressure valve of the outer bath, 9 and 11- filling line and level-meter for the inner bath, 10 and 12- filling line and level-meter for the outer bath, 13- gas exhaust and vacuum line of the inner bath, 14- gas exhaust of the outer bath, 15- connector for the LED, only used for G-MAPD testing.	39
3.12	Photograph of the set-up used to test the HFIE: 1- μ -Ar-Tube, 2- electronics for data processing and readout, 3- display of the level-meters and vacuum-probe, 4- high-voltage-supplys and boxes with 1G Ω quenching resistors, 5- ranger containing up to 200 litres of liquid Argon, 6- filter, 7- vacuum-pump.	40
3.13	Photograph of the drift-plate with the alpha-source soldered on it. . .	41
3.14	Data taken in 4 bar Argon gas with the alpha-source (left) and without (all plots in arbitrary units): top- HV(-) -2.5 kV and HV(-) -3.0 kV, middle- HV(-) -2.7 kV and HV(-) -3.2 kV, bottom- HV(-) -3.0 kV and HV(-) -3.5 kV.	42
A.1	Layout of the automatic level regulating valve in opened position (left) and closed position (right): 1- massive block, 2- bolt, 3- floater, 4- copper tube, 5- liquid noble gas.	47
A.2	Photo of the first valve prototype with the floater dismounted. . . .	48
A.3	Photo of the second valve prototype with the floater dismounted. . . .	48
A.4	Photo of the final valve with the bolt dismounted.	49
A.5	Photo of the complete final valve with washers as additional weight (left) and the bolt with Styrofoam floater (right).	49
B.1	View on the top-flange with feedthroughs to the inner (red) and outer (yellow) bath (left) and an exploded view drawing of the top part(right).	51
B.2	Technical drawing of the dewar and the cartridge (dimensions in mm).	52
B.3	The cartridge of the μ -Ar-Tube (left), mounted in the dewar (middle) and with the fully equipped top-flange mounted.	55

Bibliography

- [1] D. Renker and E. Lorenz, "Advances in solid state photon detectors". 2009 JINST 4 P04004
- [2] Russell Shoemaker Ohl, Light-Sensitive Electric Device, U.S. Patent 2402662, filed May 27, 1941, Issued June 25, 1946.
- [3] <http://en.wikipedia.org/wiki/P-n-junction>, accessed 16th of July 2010
- [4] Charles Kittel, "Einführung in die Festkörperphysik", 5. verbesserte Auflage, R. Oldenburg Verlag GmbH, München, 1980
- [5] <http://203.130.205.68/dosen/aji/embedded/transistor.htm>, accessed 17th of July 2010
- [6] K. Rajkanan, R. Singh and J. Shewchun, Absorption coefficient of silicon for solar cell calculations, Solid-State Electron. 22 (1979) 793.
- [7] R.J. McIntyre, A new look at impact ionization-Part I: A theory of gain, noise, breakdown probability, and frequency response, IEEE Trans. Electron. Dev. 46 (1999) 1623.
- [8] C.A. Lee et al., Ionization Rates of Holes and Electrons in Silicon, Phys. Rev. 134 (1964) A761.
- [9] P.P. Webb, R.J. McIntyre and J. Conradi, Properties of avalanche photodiodes, RCA Review 35 (1974) 234.
- [10] Z. Sadygov et al., Three advanced designs of micro-pixel avalanche photodiodes: Their present status, maximum possibilities and limitations, Nucl. Instrum. Meth. A 567 (2006) 70.
- [11] P. Buzhan et. al., Silicon photomultiplier and its possible applications, Nucl. Instrum. Meth. A 504 (2003) 48.
- [12] G. Charpak et. al., Nucl. Instrum. Methods A376, 29 (1996).
- [13] F. Sauli, Nucl. Instr. and Meth. A386 (1997) 531.

- [14] R. Chechik et. al., Thick GEM-like (THGEM) Detectors and Their Possible Applications, SNIC Symposium, Stanford, California – 3-6 April 2006
- [15] Fancisco Javier Rico Castro., "First Study of the Stopping Muon Sample with the ICARUS T600 Detector", 2002
- [16] Editors in Chief: K.-H.Hellwege and O.Madelung, "Landolt-Brnstein", Sub-volume 4a "Thermodynamical and Dynamical Structures of the Global Atmosphere", Springer-Verlag Berlin.
- [17] Thorsten Lux for the T2K TPC groups, A TPC for the near detector at T2K, Journal of Physics: Conference Series 65 (2007) 012018
- [18] <http://www-project.slac.stanford.edu/exo/about.html>, accessed 26th of July 2010
- [19] P.K. Lightfoot et. al., "Optical readout tracking detector concept using secondary scintillation from liquid argon generated by a thick gas electron multiplier", 2009 JINST 4 P04002
- [20] Prof. Dr. Stefan Janos, "An Introduction to Low Temperature Technique", Physikalisches Institut, Universitt Bern, 2008

Acknowledgments

I wish to thank my tutor Dr. Igor Kreslo for the very friendly and valuable collaboration and his excellent scientific support.

I gratefully acknowledge Prof. Antonio Ereditato for initiating this Master Thesis and Prof. Urs Moser for his helpful support.

I also very gratefully acknowledge the invaluable contribution of the LHEP team, especially of the workshop under the direction of Roger Hänni.

Finally i wish to warmly thank my parents for their support during my studies at the university of Bern.